Superconductor
Science and
Technology

PAPER • **OPEN ACCESS**

Design of a 75 km GW-class hybrid pipeline for the synergetic transmission of liquid hydrogen and electrical energy by high-temperature superconductivity

To cite this article: Sebastian Palacios *et al* 2025 *Supercond. Sci. Technol.* **38** 125025

OPEN ACCESS
IOP Publishing
Superconductor Science and Technology
Supercond. Sci. Technol. **38** (2025) 125025 (22pp)
https://doi.org/10.1088/1361-6668/ae2cf7

Design of a 75 km GW-class hybrid pipeline for the synergetic transmission of liquid hydrogen and electrical energy by high-temperature superconductivity

Sebastian Palacios*, Michael J Wolf, Mathias Noe, Mira Wehr and Tabea Arndt

Institute for Technical Physics (ITEP), Karlsruhe Institute of Technology (KIT), PO Box 3640, 76021 Karlsruhe, Germany

E-mail: sebastian.palacios@kit.edu

Received 8 August 2025, revised 5 December 2025
Accepted for publication 15 December 2025
Published 31 December 2025

Abstract

The transmission infrastructure for both electrical energy and hydrogen must be significantly expanded in Germany to enable climate neutrality. A hybrid pipeline can transmit both energy vectors simultaneously, efficiently, and compactly. Hybrid pipelines exploit the synergy provided by liquid hydrogen, which is used as a coolant and energy carrier, and high-temperature superconductors for the transmission of electrical energy. We present the conceptual design of a 75 km long GW-class hybrid pipeline for operation without intermediate cooling stations between Brunsbüttel and Hamburg in northern Germany. The design is based on a rare-earth barium copper oxide direct current cable and a thermally insulated rigid smooth pipe. We examine the electrical topology, cable build-up, cable behavior in the case of a short circuit, and the thermal-hydraulic design. The results lead to a hybrid pipeline with an outer diameter of less than 45 cm that can transmit 0.55–1.14 GW_t of liquid hydrogen, and two parallel coaxial monopoles that transmit 4 GW_e of electrical energy. Future research will build on the presented design to unveil the techno-economic competitiveness of this technology compared with conventional transmission alternatives.

Supplementary material for this article is available online

Keywords: hybrid pipeline, liquid hydrogen, superconducting DC cable, combined energy transmission

* Author to whom any correspondence should be addressed.

1. Introduction

Germany has set the goal of becoming climate-neutral by 2045 [1]. This goal leads to a considerable increase in electrical energy and the need to import chemical energy carriers, such as hydrogen. This result has been reported in several studies that are well-known within the German energy sector [2–5] (see figure 1). Although the scenarios in these studies quantify different amounts of energy, they all present a common trend. Germany's net electricity production in 2045 is projected to be, on average, more than twice the level recorded in 2022. Throughout this paper, the lower heating value of hydrogen is used as the basis for all energy content comparisons[1]. This implies that Germany will require between 213 and 694 TWh_t of hydrogen per year. This amount of energy is comparable to the electrical energy output reported in 2022, which was 542 TWh_e. In that same year, the annual hydrogen demand was limited to just 0.1 TWh_t.

Consequently, large network extensions are required in the electrical grid at all voltage levels [6]. For the natural gas network, considerable modifications are necessary to enable hydrogen transmission and distribution [7]. At present, both networks are planned separately without interconnections. This work shows that a hybrid pipeline that transmits electrical and chemical energy is far more compact and highly efficient. In this context, the main research question of this paper is: How can a hybrid pipeline transmit electrical energy and hydrogen synergetically by considering a case study in Germany?

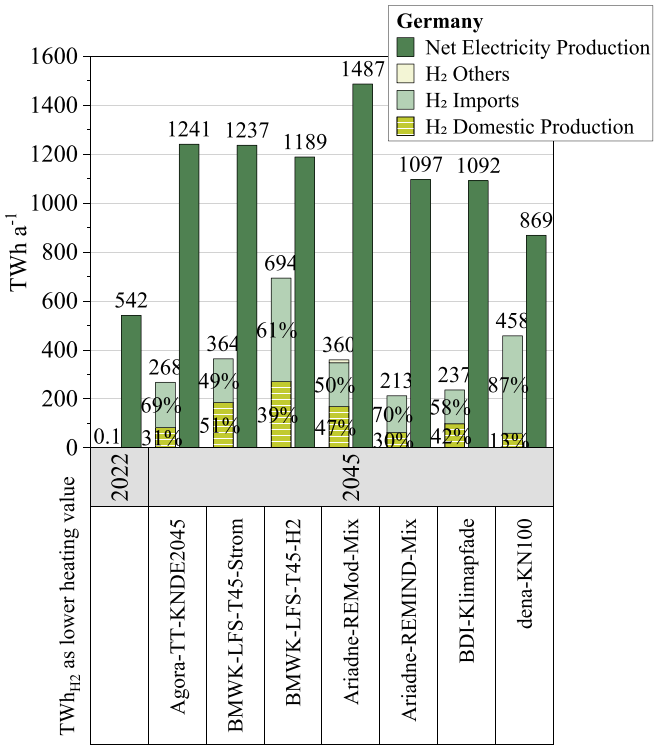

Figure 1. Net electricity production and hydrogen (H_2) demand in Germany in 2022 and 2045 according to multiple studies on behalf of different German political entities. The hydrogen sources are divided into imports, domestic production, and others. The lower heating value of hydrogen is considered. Own design based on [2–5].

1.1. Energy production and import

To a major extent, the generation of electrical energy and hydrogen for Germany will take place far from the consuming areas. For example, the German law stipulates that by 2045, 70 GW_e of offshore wind power will be connected to the high-voltage grid and transmitted mainly from the north to the south of the country [8]. The studies in figure 1 have concluded that hydrogen produced in Germany will be less cost-competitive than hydrogen imports from countries with a larger potential for low-cost renewable energy sources. This is principally due to lower full-load hours of renewable energy systems in Germany, which are caused by less favorable weather conditions. Therefore, hydrogen will be largely imported (see figure 1), as confirmed in the Import Strategy of the German Government [9]. Multiple analyses have shown that hydrogen imports may be by pipeline from inside Europe [10], but also by ship from other continents [11–13].

Hydrogen is usually produced in a gaseous state at low pressures [14]. Gaseous hydrogen has a low volumetric energy density (2.8 Wh l^{-1} at 293.15 K and 100 kPa) [15]. For its transport overseas, gaseous hydrogen must be liquefied or converted at the export location to increase its energy density. Some conversion options include, e.g., ammonia, LOHC, and methanol. In comparison, hydrogen liquefaction is not only useful for increasing its energy density, but it also implies the import of high-purity hydrogen and a high-value cryogenic temperature level.

1.2. Energy use

Three properties make liquid hydrogen very valuable for several types of consumers:

- high energy density (32.9 kWh kg^{-1} and 2.3 kWh l^{-1} for parahydrogen[2] at 20 K and 100 kPa [15]),
- high purity ($\geqslant$ 99.995 % by volume [16, 17]), and
- cryogenic temperature level (approx. 253 °C or 20 K [15]).

The high energy density of liquid hydrogen is especially beneficial for decarbonizing parts of the aviation sector [18], but it is also useful for maritime vessels [19] and long-range trucks [20] to phase out fossil fuels. The high purity of liquid hydrogen has a special value for parts of the manufacturing industry,

[1] The lower heating value, also called net heating value, is calculated by subtracting the latent heat of vaporization of water vapor from the gross heating value, which is the amount of heat generated by the total combustion of a unit quantity fuel [124].

[2] At ambient temperature and higher, the ratio of orthohydrogen to parahydrogen is approximately 3 : 1. As the temperature decreases, the balance shifts progressively towards parahydrogen. At 20 K, the ratio of orthohydrogen to parahydrogen is approximately 0.002 : 0.998 [125].

for example for the chip industry [21], but it also presents an efficiency and lifespan benefit for fuel cells [22]. In addition, regasified liquid hydrogen can be employed by large hydrogen demand centers, such as for steelmaking and chemicals [23].

The use of the cryogenic temperature level of liquid hydrogen provides several advantages. Liquid hydrogen at temperatures of approximately 20 K enables the use of high-temperature superconductors (HTSs) without additional cooling. Superconducting cables can be utilized to expand the electrical grid to supply growing and emerging consumers with electrical energy, such as in Munich [24] and Paris [25]. Superconducting motors [26] and generators [27] cooled by liquid hydrogen also decrease the dependence on copper and permanent magnets. The cryogenic temperature level of liquid hydrogen can be used for electricity production by recovering cold energy, for example, when combining the Brayton and Rankine cycles [28] or potentially for cooling in the chemical, process, and food industries [29].

Despite decades of use of liquid hydrogen as a fuel in aerospace and as a source of high-purity industrial gas, the experienced gained is only partly useful for non-industrial applications. However, projects such as the liquid-hydrogen *GenH2* truck from Daimler 2023 [30], the *Hydrogen Energy Supply Chain (HESC)* between Australia and Japan 2022 [31], and the EU project *Pre-normative REsearch for Safe use of Liquid HYdrogen* (*PRESLHY*) 2017–2021 [32] have provided increasing evidence that, when liquid hydrogen is handled professionally and its specific characteristics are considered in the system design, liquid hydrogen is as safe as other fuels. For example, even though hydrogen is extremely diffusive and it has the lowest minimum ignition energy, spontaneous ignition is extremely unlikely, while the combustible air-hydrogen cloud rapidly dilutes. Although materials in contact with liquid hydrogen must be resistant, e.g. to embrittlement, and they must withstand wide temperature ranges between 20–293 K and pressure ranges, for example, between 100–1 200 kPa, several materials, such as metal alloys, fiber-reinforced composite materials, and laminated structures have demonstrated adequate performance under such operating conditions [33].

Consumers of electrical energy can be divided into the following sectors: industry, households, non-residential buildings (trade, commerce, and services), and transport [4]. The progressive electrification of energy systems causes an increase in electricity production from 2022 to 2045, as shown in figure 1. Electrification is for example driven by emerging consumers such as electric vehicles and heat pumps, according to the studies in figure 1 [2, 3, 5]. Therefore, the consumption of electrical energy will be concentrated in highly populated regions, and where a relevant share of industry and non-residential buildings are located.

1.3. Energy transmission

Figure 2 shows a schematic of the production, use and transport of liquid hydrogen and electrical energy using a hybrid pipeline on a GW-scale. A hybrid pipeline is composed of a thermally insulated pipeline and a superconducting cable. To date, liquid hydrogen has been tested for cooling magnesium

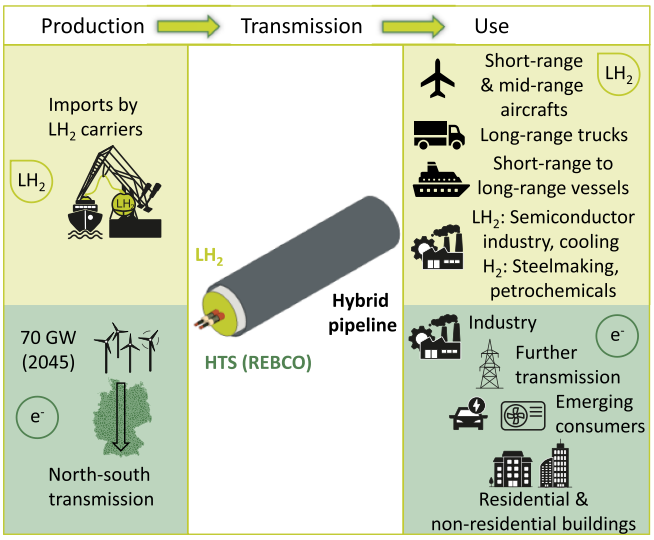

Figure 2. Basic principle of the production, transmission, and use of liquid hydrogen (LH_2) and electrical energy (e^-) when transmitted by a hybrid pipeline in Germany. The high-temperature superconductor (HTS) for the cable is a rare-earth barium copper oxide (REBCO). The liquid hydrogen is mainly used in the transport sector and in parts of the manufacturing industry. Regasified hydrogen (H_2) can be used by large hydrogen consumers, e.g. for steelmaking. The use of electrical energy is mainly driven by the industry and by emerging consumers like electric vehicles or heat pumps.

diboride cables in 10 m long [34] and 30 m long [35] corrugated, flexible pipelines with mass flow rates of up to 250 g s^{-1} (30 MW_t).[3] However, liquid hydrogen has not been used in non-corrugated, rigid hybrid pipelines as an energy carrier in bulk. Recently, a 10 m [36] and 30 m long [37] prototype of superconducting energy pipelines using bismuth strontium calcium copper oxide were built and tested, but they used liquefied natural gas instead of liquid hydrogen as the chemical energy carrier.[4] A 10 m long prototype of a non-corrugated, rigid liquid hydrogen hybrid pipeline, using rare-earth barium copper oxide (REBCO) tapes, is under construction at Karlsruhe Institute of Technology (KIT), Germany, in the framework of the *TransHyDE* project *AppLHy!* [38].

The use of liquid hydrogen transfer lines is well known in industrial facilities, especially due to the NASA space program [39]. Liquid hydrogen transfer lines are commercially available, e.g. from [40, 41]. Their application for energy distribution has been proven on small scale, for example, in 2010, during the *icefuel* project. In the study, a low mass flow rate of

[3] The magnesium diboride projects were made in the framework of the program 'Basic Principles of Development of Power Systems and Technologies, Including High Temperature Superconductors' supported by the Russian Academy of Sciences and JSC 'Rosseti'—Russian Grids.

[4] The 10 m superconducting energy pipeline with BSCCO and liquefied natural gas was supported by the National Key Research and Development Program of China and the Science and Technology Project of the State Grid Corporation of China, while the 30 m liquefied natural gas-BSCCO pipeline was made in the framework of the China Electric Power Research Institute and the Institute of Electrical Engineering of the Chinese Academy of Sciences.

10 MW_t, pipe diameter of approximately 20 mm, and heat load less than 1 W m^{-1} predicted transport distances of up to 10 km without intermediate cooling stations [42]. Owing to the large amount of hydrogen needed to reach climate neutrality, larger mass flow rates are required today.

Conceptually, hybrid pipelines with HTS and liquid hydrogen have already been presented, initially only as a basic idea in the early 2000's by the founder of the US American Electric Power Research Institute, Starr [43]. A first basic design was presented by the US American energy consultant Grant [44]. Later studies have included some general technical background, such as the bachelor's thesis of Prats-Campmany from the Superior Technical School of Industrial Engineering of Barcelona [45], or their long-term, continental-scale potential, as in two works of Qin *et al* from the Xi'an Jiaotong University, supported by the National Natural Science Foundation of China [46, 47]. More specific technical designs have been developed, but these designs consist of REBCO and liquid hydrogen with liquid natural gas as a refrigerant for the electric shielding outer layer, as in the works of Wang *et al* [48] and Jin *et al* from the Tianjin University [49]. Other more specific technical designs consist of magnesium diboride superconductors and liquid hydrogen, as in the doctoral thesis of Trevisani from the University of Bologna [50], and in the works of Yamada *et al* from Japan's National Institute for Fusion Science [51], Savoldi *et al* from the Polytechnic University of Turin [52], Bracco *et al* from the University of Genoa [53], and Bruzek *et al* from ASG Superconductors within the ongoing European project SCARLET [54, 55]. Compared with magnesium diboride, REBCO provides a higher current carrying capacity and a larger temperature range of operation, which can result in lower material requirements or a wider safety margin [56, 57]. Recently, the design and economic evaluation of a hybrid pipeline with REBCO and liquid hydrogen was presented by Fu *et al* from the Tongji University, within the framework of the Young Elite Scientists Sponsorship Program by the China Association for Science and Technology, and the National Natural Science Foundation of China. However, the transmission scheme was for railway transportation and not for the transmission grid [58].

This paper presents the case study and conceptual design of a GW-class 75 km long hybrid pipeline without intermediate cooling stations, based on a REBCO direct current (DC) cable and a liquid hydrogen non-corrugated rigid pipe. An analysis of the future availability and demand for both energy carriers in Germany leads to a case study between Brunsbüttel and Hamburg in northern Germany. The requirements for reliable and safe cable operation, even in the case of an electric fault, will be discussed. Based on this, a conceptual design will be proposed.

2. Definition of the case study and requirements

In Germany, Brunsbüttel is an industrial and port town in the North Sea area that will become a major interconnection point for both electrical energy and hydrogen. Several offshore wind farms in the North Sea will deliver at least 3 GW_e of electrical energy to the Brunsbüttel area [59]. Further electric power is planned to be transmitted from the north to the south of Germany over this region [60–62]. Since 2023, a liquefied natural gas floating storage and regasification unit is located in Brunsbüttel [63]. A stationary terminal will be used in the future to import hydrogen [64]. These multiple reasons make Brunsbüttel appropriate for this case study.

Table 1. Requirements for selected case study Brunsbüttel-Hamburg.

Parameter	Value
Length (*len*)	75 km
Electric rated power (P_0)	4 GW_e
Hydrogen demand in Hamburg	From 0.62 GW_t (5.13 kg s^{-1}) to 0.87 GW_t (7.22 kg s^{-1})

Hamburg is a large city where a wide spectrum of electricity and hydrogen consumers is concentrated: industry, residential areas, non-residential buildings, and several logistic centers, from short-range to long-range transportation. Hamburg is home to the largest seaport in Germany [65], the largest airport in the north of the country [66] and large logistic companies [67]. The industrial sector comprises steel [68], aircraft [69, 70], chip manufacturers [71], and other chemical plants [72]. The city has more than 5 million inhabitants in the metropolitan area [73]. We assume that the hybrid pipeline delivers liquid hydrogen in bulk to a centralized location in Hamburg, where the largest consumer of liquid hydrogen is located, and from which other smaller consumers can be supplied, for example, by trailers.

Table 1 shows the requirements of the selected case study, Brunsbüttel-Hamburg. We selected a rated electric power P_o of 4.0 GW_e. The assumption is based on the transmission power of current high-voltage DC projects between northern and southern Germany, and the large demand for electrical energy transmission until 2045. A study from the Hamburg Ministry of Economic Affairs and Innovation, based on interviews with industry stakeholders, predicts an import demand of hydrogen of 5.4 TWh a^{-1} and a total hydrogen demand of 7.6 TWh a^{-1} in 2030 in Hamburg (0.62 GW_t and 0.87 GW_t, respectively) [74]. This is equivalent to a continuous mass flow range between 5.13 kg s^{-1} and 7.22 kg s^{-1} (18.5 t h^{-1}–26.0 t h^{-1}). The German Economic Institute forecasts a hydrogen demand in Hamburg of 1.64 GW_t in 2035 (13.67 kg s^{-1} or rather 49.2 t h^{-1}), and 3.73 GW_t in 2045 (31.05 kg s^{-1} or 111.8 t h^{-1}) [75, 76]. We assume a hydrogen demand between 0.62 GW_t and 0.87 GW_t as a conservative hypothesis.

3. Conceptual design of the hybrid pipeline

Figure 3 presents the proposed side view of the hybrid pipeline. Two parallel DC coaxial monopoles transmit the electrical energy. Each cable has copper as a mechanical and electrical stabilizer with radii $r_{1,cu}$ and $r_{2,cu}$ in both the inner and outer phases, respectively. High-temperature superconducting REBCO tapes are in contact with each copper layer. The radius of the outer side of the REBCO tape in the inner

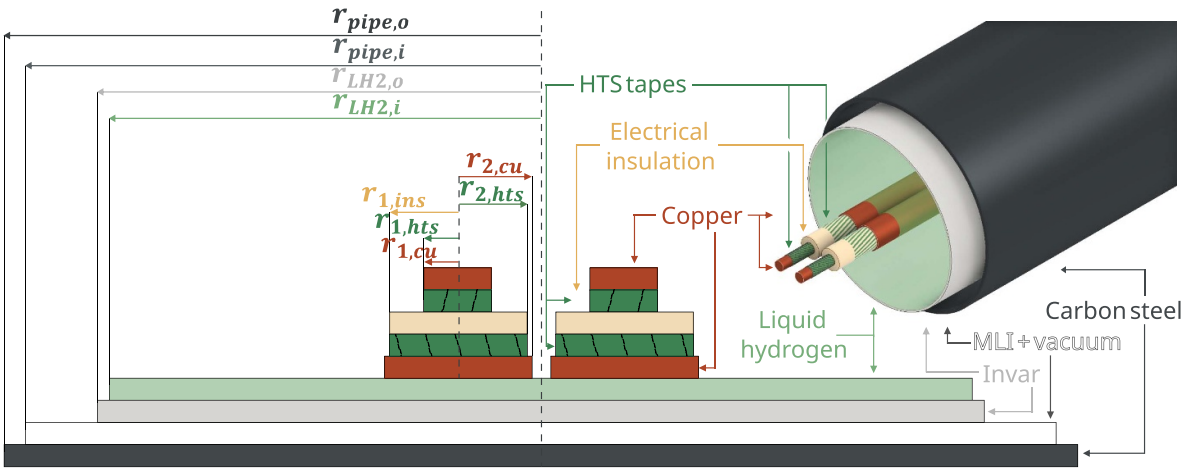

Figure 3. Side view of hybrid pipeline: $r_{\mathrm{pipe,o}}$ and $r_{\mathrm{pipe,i}}$ are the outer and inner radii of the outer pipeline correspondingly (warm). $r_{\mathrm{LH2,o}}$ and $r_{\mathrm{LH2,i}}$ are the outer and inner radii of the liquid hydrogen conducting pipeline, respectively. Between the outer and the inner pipeline, multi-layer insulation (MLI) is in vacuum. $r_{2,\,\mathrm{cu}}$ and $r_{2,\,\mathrm{hts}}$ are the radii in the outer phase of the copper stabilizer and of the high-temperature superconductor (HTS) layer in the order given. The radius of the electrical insulation between the inner and the outer phases is $r_{1,\,\mathrm{ins}}$. Equivalently, $r_{1,\,\mathrm{hts}}$ and $r_{1,\,\mathrm{cu}}$ are the radii of the inner HTS layer and of the inner copper stabilizer.

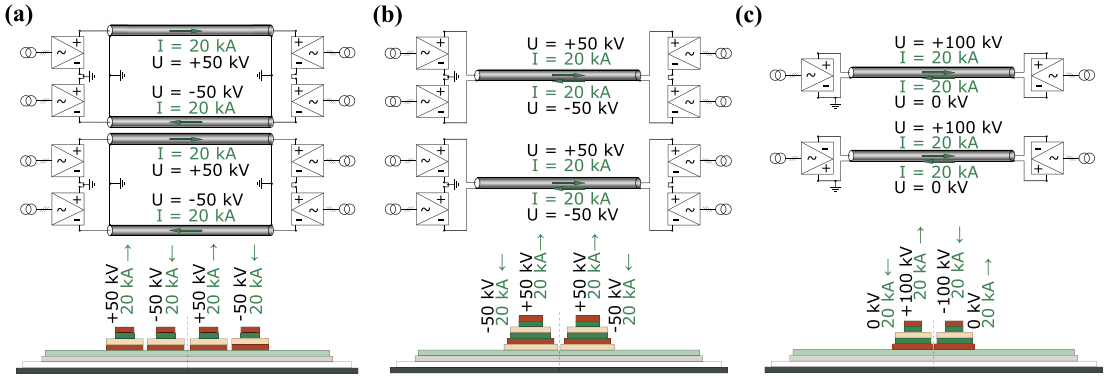

Figure 4. Considered topologies: (a) two parallel rigid bipoles without metallic return; (b) two parallel coaxial rigid bipoles without metallic return; (c) two parallel coaxial monopoles with metallic return. Topology (c) was selected.

phase is $r_{1,\mathrm{hts}}$ and $r_{2,\mathrm{hts}}$ is the corresponding radius in the outer phase. The REBCO tapes carry the electrical current under rated operation conditions. A layer of electrical insulation with an outer radius $r_{1,\mathrm{ins}}$ electrically separates both the inner and outer phases. The electrical insulation is made of Kapton® or polypropylene laminated paper (PPLP), as it will be discussed in section 3.2. The outer copper and HTS layers are grounded.

Around the cables, liquid hydrogen is transmitted in a double-walled, rigid, and smooth pipe. The inner pipe with inner radius $r_{\mathrm{LH2,i}}$ and outer radius $r_{\mathrm{LH2,o}}$ is made up of invar (36 % Ni–Fe) to reduce thermal contraction due to large temperature differences. Invar's coefficient of thermal expansion is approximately one-tenth of that of steel [77]. Approval for pressure equipment might be feasible, as invar is already being used, for example, for liquefied natural gas pipes and tanks [78, 79]. Some studies have shown that invar is resistant to hydrogen embrittlement [80, 81]. The thermal insulation between the inner and the outer pipes is comprised of vacuum and multi-layer insulation. The outer pipe is made of carbon steel, and has inner and outer radii $r_{\mathrm{pipe,i}}$ and $r_{\mathrm{pipe,o}}$, respectively.

3.1. Electrical topology

Figure 4 shows the electrical topologies considered. First, we examined a topology similar to that of the currently planned conventional underground high-voltage DC cables [82], which are composed of two parallel rigid bipoles without a metallic return. Each rigid bipole has two cables and each cable has a grounded cable shield. This topology would have led to four cables of 50 kV, 20 kA, 1 $\mathrm{GW_e}$ each, as shown in figure 4(a). However, such a topology not only increases the space demand. For superconducting cables, the resulting cable layout generates a large magnetic field outside each cable. Some consequences are a reduction in the critical current, mechanical challenges due to Lorentz forces, and a considerable magnetic field extending into the environment.

To cancel the magnetic field outside the cables, another option was a couple of coaxial rigid bipoles without a metallic return (see figure 4(b)). This would mean two coaxial cables of 2 GW_e each ($\pm$ 50 kV, 20 kA), where the corresponding outer phase is not grounded. The resulting cable layout increases the cable diameter owing to the necessity of an additional electric insulation layer outside the cable. The mechanical flexibility of the cable decreases, complicating its transport. Since the outer phase is not grounded, induced voltage originates in the case of current changes. In addition, to the best of our knowledge, there has been no experience with this cable layout outside a laboratory.

There are multiple advantages to the cable layout given by the following selected topology: two parallel coaxial monopoles with metallic return (2 GW_e each, see figure 4(c)). Because the outer phase is grounded, there is no need for an electric insulation layer outside the cable. The diameter of each cable is smaller, which facilitates its transport in drums. Grounding the outer phase limits the induced voltages in the case of a current change. Outside the cables, there is practically no magnetic field, because of the cancellation caused by the current flowing in opposite directions in the inner and the outer phases (see section 3.3).

In all considered topologies, if one cable is out of operation, only 2 GW_e of 4 GW_e is disconnected. The proposed topology with two parallel monopoles in the pipeline improves the maintainability, redundancy, and supply security in the case of a monopole outage. A similar topology has been suggested in [54]. However, our study does not investigate the outage of the complete hybrid pipeline, for example, owing to the lack of liquid-hydrogen flow. The authors of [53] propose a parallel copper line to achieve redundancy. In [52], multiple small hybrid pipelines are preferred.

To transmit 4 GW_e, we opted for a rated voltage U_0 of 100 kV, and a rated current I_0 of 20 kA. However, a design such as $\pm$ 50 kV and 40 kA would have also been feasible. A cable rated at $\pm$ 100.0 kV is categorized as part of the high-voltage power grid, whereas a cable rated at $\pm$ 50.0 kV falls within the medium-voltage range [83]. One advantage of medium voltage is the smaller size of the converter stations [84]. This can potentially lower the cost of the entire electric system. However, increasing the rated voltage from $\pm$ 50.0 kV to $\pm$ 100.0 kV decreases the rated current from 40 to 20 kV. Therefore, with a lower rated current, less superconductor amount is required. In this manner, the potential costs of the cable are reduced. The effect of high voltage and medium voltage on the amount of superconductor will be presented in section 3.2.

The minimum self-field critical current $I_{c,min}$ is chosen to be 25.0 kA to provide a safety factor of 0.8 to the rated current I_0 of 20 kA. The calculation method of the self-field critical current in the inner phase $I_{c,1}$ and in the outer phase $I_{c,2}$ will be presented in section 3.3. Even though the rated operation with liquid hydrogen would be at approximately 20 K, the design temperature T_{des} was considered to be 30 K as a conservative assumption in the case of higher operation temperatures.

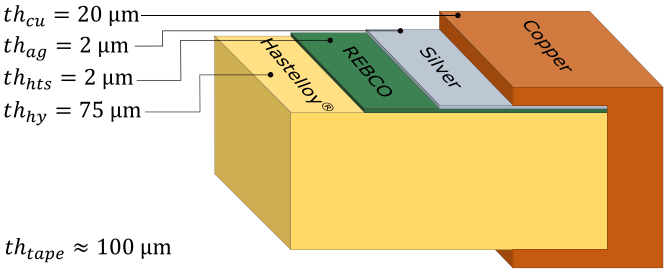

Figure 5. Thickness of each layer in the REBCO tape to scale. The total tape thickness th_{tape} comprises about 100 µm. The total thickness of the copper layer th_{cu} is 20 µm, from which 10 µm are above and 10 µm are below the other materials.

3.2. Cable build-up

The radius of the inner copper stabilizer plays a major role in the design of the cable. It determines the maximum number of REBCO tapes that can be wound per layer on top of the core, and it largely characterizes the electrical behavior of the cable in the case of a short circuit. Our design leads to an inner copper stabilizer with a radius $r_{1,cu}$ of 14.2 mm. This value is well in the range of the typical radii of copper cores between 5 mm and 20 mm [85]. The analysis that led to this result will be discussed in sections 3.3 and 3.4. In this section, we first discuss the physical consequences of the size of the inner copper stabilizer.

The number of tapes per layer in the inner phase $N_{tapes,1}$ is calculated using equation (1). This is composed of the geometric equation for the surface of a circle and the trigonometric function owing to the lay angle of the tape:

$$N_{tapes,1} = \left\lfloor \frac{2 \cdot \pi \cdot r_{1,cu}}{w_{tape} / \cos(a_1)} \right\rfloor . \tag{1}$$

Assuming a radius $r_{1,cu}$ of 14.2 mm, a typical lay angle for the inner phase a_1 of 15° [85], and a tape width w_{tape} of 4.0 mm, the result is a number $N_{tapes,1}$ of 21 tapes.

Figure 5 shows the materials that comprise the superconducting tape and their corresponding thicknesses. The total thickness of the tape th_{tape} is of about 100 µm. These dimensions are based on the technical sheet provided by the manufacturer, which is Fujikura Ltd. For the sake of simplicity, we neglect buffer layers–like magnesium oxide–that only have a share of about 0.7 % in the tape thickness. Assuming one layer of REBCO tapes in the inner phase, the outer radius of the tape in the inner phase is $r_{1,hts}$ and is given by the radius of the copper stabilizer $r_{1,cu}$ plus the thickness th_{tape}, i.e. 14.3 mm.

The electric field inside the coaxial cable is calculated using the equation

$$E(r) = \frac{U}{r \cdot \ln\left(\frac{r_a}{r_i}\right)}, \tag{2}$$

where E is the electric field at radius r of a cylindrical capacitor with an outer radius r_a and inner radius r_i [86]. We aim for a

maximum electric field E_{lim} of 10 kV mm^{-1} during rated operation conditions. The selection of this value will be discussed later in this section. The highest electric field occurs when the radius r is equal to the inner radius r_{i}. The outer radius of the insulation $r_{1,\mathrm{ins}}$ is calculated by solving equation (2) for the outer radius r_{a}, that is,

$$r_{1,\mathrm{ins}} = r_{1,\mathrm{hts}} \cdot \mathrm{e}^{\frac{U_0}{E_{\mathrm{lim}} \cdot r_{1,\mathrm{hts}}}}, \tag{3}$$

where the outer radius r_{a} has been replaced by the outer radius of the insulation $r_{1,\mathrm{ins}}$, the electric field E by the maximum electric field E_{lim}, the voltage U by the rated voltage U_0, and the inner radius r_{i} by the outer radius of the tape $r_{1,\mathrm{hts}}$. The result is the outer radius of the insulation $r_{1,\mathrm{ins}}$ equal to 28.8 mm.

Setting the maximum electric field E_{lim} as 10 kV mm^{-1} is an assumption based on the design of other high-voltage superconducting and conventional cable systems, such as those named in [87] at 420 kV and 380 kV, respectively. This assumption can be validated with the following considerations. Currently, there are no official standards for determining the testing voltage of paper-lapped high-voltage DC cables under cryogenic conditions [88]. If the standard for extruded insulation materials is applied, the test voltage U_{T} should be 1.85 times the nominal voltage U_0 of 100 kV, i.e. the test voltage U_{T} should be 185 kV [89]. In addition, a breakdown voltage E_{b} of 20 kV mm^{-1} has been previously assumed for the DC operation of paper insulation in liquid hydrogen [85]. These assumptions would lead to a slightly smaller insulation radius than $r_{1,\mathrm{ins}}$ in equation (3), that is,

$$r_{1,\mathrm{ins}} > r_{1,\mathrm{hts}} \cdot \mathrm{e}^{\frac{U_{\mathrm{T}}}{E_{\mathrm{b}} \cdot r_{1,\mathrm{hts}}}}. \tag{4}$$

The material of the electric insulation is assumed to be similar to those used for superconducting cables cooled with liquid nitrogen, such as Kapton® or PPLP. It has been shown that the dielectric strength of liquid hydrogen at 20 K is slightly higher than that of liquid nitrogen at 77 K [90]. However, the dielectric properties of materials such as Kapton® and PPLP in liquid hydrogen still require experimental verification. So far, only the suitability of using crepe insulation paper has been demonstrated in liquid hydrogen up to 50 kV DC [35]. The authors of that study did not specify which type of crepe insulation paper was used.

The maximum number of tapes per layer in the outer phase $N_{2,\mathrm{tapes}}$ is calculated similarly to equation (1). However, it is possible to choose between three layout types. The three types are presented in figure 6. Type I has the same number of tapes in the inner and outer phases, but the lay angle in the outer phase a_2 is larger than the lay angle in the inner phase a_1, so that the outer phase can be fully wound. Type II has the same lay angle in the inner and outer phases, but the number of tapes in the outer phase $N_{2,\mathrm{tapes}}$ is larger than that in the inner phase $N_{1,\mathrm{tapes}}$ to be fully wound. Type III has the same number of tapes and the same lay angle in both phases; however, the outer phase is not fully wound. Several DC and alternating current (AC) superconducting cable projects built so far have used layouts based on type II [91–95]. However, the main advantage of type III is the significantly lower amount of superconductor

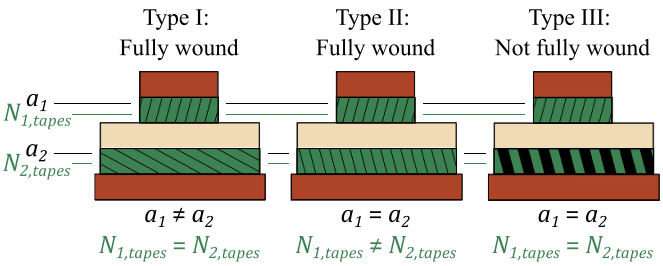

Figure 6. Possible layout types for the tapes in the outer phase. Type I and type II are fully wound, while type III is not. The angle in the inner phase a_1 and the angle in the outer phase a_2 is equal or not depending on the presented type. Also, the number of tapes in the inner phase $N_{1,\mathrm{tapes}}$ and number of tapes in the outer phase $N_{2,\mathrm{tapes}}$ might be equal or not. Type III was selected.

compared to types I and II. This comparison and a summary of the build-up of the cable are presented in table 2.

Designs A, B, and C have the same rated voltage U_0 of $\pm$ 100 kV, and the same rated current I_0 of 20.0 kA. Design D presents a lower rated voltage U_0 of $\pm$ 50 kV, and a higher rated current I_0 of 40.0 kA. The specifications in the inner phase of designs A, B, and C are equal; however, they differ in the layout of the outer phase. Design A is based on type III, while design B bears on type II, and design C bears on type I. Design A requires approximately 35 % less superconductor than design B and design C.

Compared to design D, design A requires approximately 52 % fewer superconductor, even though both designs are based on type III. This is mainly due to the larger rated current I_0 in design D, which increases the number of tapes $N_{1,\mathrm{tapes}}$ in the inner phase and $N_{2,\mathrm{tapes}}$ in the outer phase to reach a high minimum critical current in the inner phase $I_{\mathrm{c},1}$ and outer phase $I_{\mathrm{c},2}$ (more details in section 3.3). The radii of the copper stabilizer in the inner phase $r_{1,\mathrm{cu}}$ and outer phase $r_{2,\mathrm{cu}}$ are larger in design D caused by the higher rated current I_0 too. However, the total cable surface A_{cable} is smaller in design D, because the thickness of its electric insulation is thinner owing to the lower rated voltage U_0.

Table 2 introduces the gap between tapes in the inner phase $g_{1,\mathrm{tapes}}$ and outer phase $g_{2,\mathrm{tapes}}$. Even though the gap $g_{2,\mathrm{tapes}}$ in design A is larger than that in the other designs, the magnetic field outside the cable is still sufficiently low to be negligible (see section 3.3). A more detailed quantitative analysis of this effect has been partially presented [96]. As long as there are any or negligible AC losses, we propose design A for the conceptual design in this case study, because of the considerably lower total amount of superconductor. It should be noted that no cable projects are known to use type III layouts.

3.3. Validation of the amount of superconductor

The amount of superconductor per phase is properly selected if it can conduct the minimum critical current $I_{\mathrm{c,min}}$ of 25.0 kA. To validate this, we calculate the self-field critical current provided by the selected number of tapes $N_{1,\mathrm{tapes}}$ and $N_{2,\mathrm{tapes}}$. We consider the magnitude and angle of the magnetic

Table 2. Comparison of different cable build-up alternatives.

Parameter	Design A (selected)	Design B	Design C	Design D
P_0		4.0 GW_e		
U_0		± 100.0 kV		± 50.0 kV
I_0		20.0 kA		40.0 kA
$I_{c,min}$		25.0 kA		50.0 kA
w_{tape}		4.0 mm		4.0 mm
th_{tape}		0.1 mm		0.1 mm
$r_{1,cu}$		14.2 mm		20.0 mm
$r_{1,hts}$		14.3 mm		20.2 mm
$r_{1,ins}$		28.8 mm		25.9 mm
$r_{2,hts}$		28.9 mm		26.1 mm
$r_{2,cu}$		30.9 mm		30.3 mm
A_{cable}		2 999.7 mm^2		2 889.7 mm^2
$N_{1,tapes}$		21		44
$g_{1,tapes}$		0.108 mm		1.571 mm
$N_{1,layers}$		1		2
a_1		15.0°		15.0°
$I_{c,1}$		25.6 kA		50.7 kA
Outer phase layout	Type III	Type II	Type I	Type III
$N_{2,tapes}$	21	43	21	44
$g_{2,tapes}$	4.47 mm	0.06 mm	0.00 mm	3.25 mm
$N_{2,layers}$	1	1	1	2
a_2	15.0°	15.0°	62.3°	15.0°
$I_{c,2}$	−25.1 kA	−26.0 kA	−26.0 kA	−50.1 kA
Total superconductor amount	6 523 km	9 939 km	10 042 km	13 666 km

field caused by the cable itself during rated operation at a conservative design temperature T_{des} of 30 K.

REBCO tapes of the selected HTS manufacturer were sent to the Robinson Research Institute in New Zealand to measure the critical current. Appendix A presents the measured critical currents for the purchased HTS tapes. It shows the dependencies on temperature, field angle, and magnetic flux density.

We employ a 2D analysis of the cross section of the superconducting cable, as shown in figure 7(a). Each of the REBCO tapes is discretized into nodes perpendicular to the cross section. Every current node has a position $\vec{r}$ and a normal vector $\vec{n}_c$ with information regarding the tape direction in the layer. We assume 10 nodes per mm width of a 4 mm wide REBCO tape (see figure 7(b)). The total number of nodes N_{nodes} is calculated using the following equation:

$$N_{nodes} = 10\frac{\text{nodes}}{\text{mm}} \cdot w_{tape} \cdot (N_{1,layers} \cdot N_{1,tapes} + N_{2,layers} \cdot N_{2,tapes}) \tag{5}$$

Therefore, design A has 1680 nodes. To calculate the self-field critical current in each node, we use the critical current measurements I_c under a magnetic field $\vec{B}$ presented in figure A.1, appendix A. To use these data for design purposes, the magnetic field dependence was fitted to the following elliptical model [97]:

$$I_c\left(\vec{B}\right) = I_{c0} / \left(1 + \sqrt{k^2 B_{\parallel}^2 + B_{\perp}^2}/B_c\right)^{\beta}. \tag{6}$$

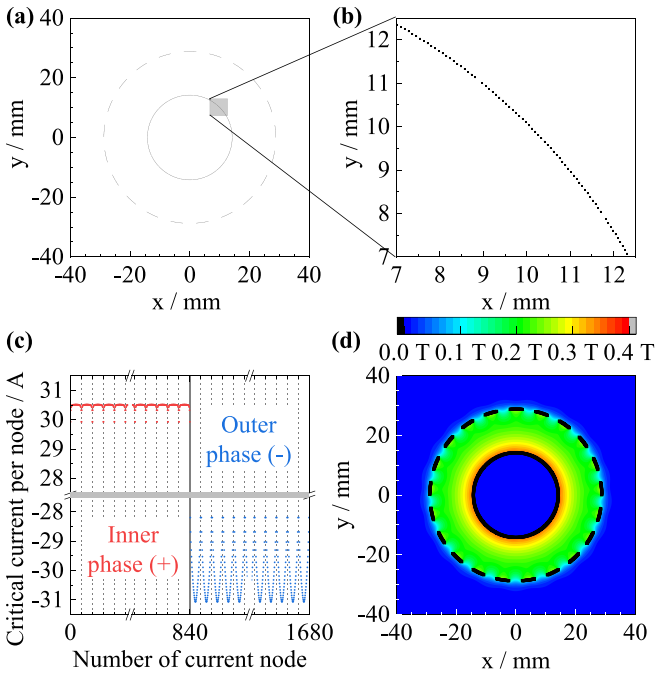

Figure 7. Determination of the critical current of a high-temperature superconducting cable for the selected design: (a) discretization of the cable cross-section into current nodes; (b) magnification of the gray section in (a); (c) calculated critical currents of the considered 1680 current nodes. (d) Flux density distribution in and around the cable.

Table 3. REBCO tape parameters derived from the data presented in figure A.1.

Parameter	Value ($T_{\text{des}} = 30$ K)
I_{c0}	316.6 A $\text{mm}^{-1}_{\text{width}}$
k	0.2871
β	0.89076
B_{c}	1.21901 T

The values of the fitting parameters I_{c0}, k, β, and B_{c} are presented for T_{des} in table 3. The magnetic fields $B_{\parallel}$ and $B_{\perp}$ are the parallel and perpendicular components of the magnetic field $\vec{B}$, respectively.

In the case of a sufficiently long, straight thread, the magnetic field $\vec{B}_l$ at location $\vec{r}_l$ is determined as

$$\vec{B}_l\ (I_i,\ \vec{r}_l,\ \vec{r}_i) = \frac{\mu_0\, I_i}{2\,\pi\ \|\vec{r}_l - \vec{r}_i\|^2} \begin{pmatrix} y_i - y_l \\ x_l - x_i \end{pmatrix}, \tag{7}$$

where I_i is the self-field critical current of a specific node i at location $\vec{r}_i$. Using equation (7), we calculate the magnetic field vector caused by each node on the other nodes. This leads to a total magnetic field profile caused by all the nodes. The total field profile is used in the elliptical model (6) to calculate the self-field critical current of each node I_i. Here, the polarity of both phases is considered: the inner phase (+) and the outer phase (−).

The preceding steps are iterated until self-consistent magnetic flux densities and critical current distributions are determined, since the initial input parameter of the self-field current for every node I_i in equation (7) is defined as the tape parameter I_{c0}. The calculation typically converges after approximately seven iterations, until a relative current change of 10^{-7} is fulfilled as the convergence criterion. Subsequently, post-processing follows, in which the flux density distribution is also calculated at arbitrary locations based on equation (7). The resulting magnetic field distribution is shown in figure 7(d). The magnetic field outside the cable cancels and can be neglected. The highest magnetic field magnitude of approximately 0.34 T is close to the inner phase.

The sum of the self-field critical currents of the nodes are the self-field critical currents $I_{\text{c,1}}$ and $I_{\text{c,2}}$ in the corresponding phases. The results are shown for each design in table 2. The values of the self-field critical currents $I_{\text{c,1}}$ and $I_{\text{c,2}}$ confirm that the amount of superconductor is sufficient because the values are larger than the corresponding minimum critical current $I_{\text{c,min}}$.

Figure 7(c) shows the critical currents of the tapes. It can be observed that at the ends of the tapes, the critical current is reduced compared to the center of the tape due to the increasing vertical magnetic field components, as expected. This effect is amplified in the outer phase (−), owing to the larger gap between the tapes. The absolute values in figure 7(c) align with the expectations from the tape measurements at 30 K and magnetic flux densities below 0.2 T of the Robinson Research Institute in figure A.1, appendix A, that is, approximately 30 A node^{-1} corresponds to approximately 3000 A cm^{-1}, considering 10 nodes per mm width.

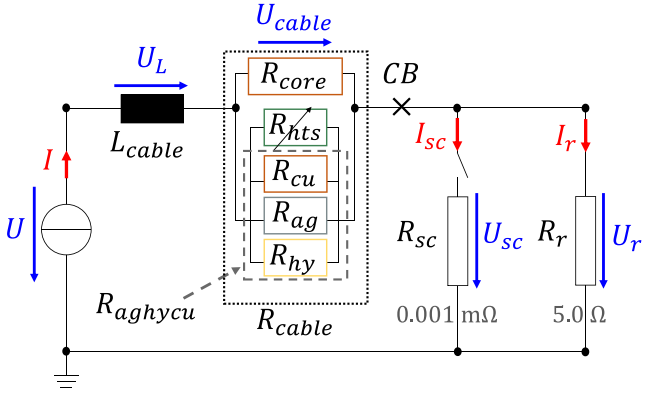

Figure 8. Circuit representation of a monopole cable for the case of a short circuit, where U is the source voltage, I is the source current, U_{L} is the voltage over the cable inductance L_{cable}, U_{cable} is the voltage over the equivalent cable resistance R_{cable}, U_{sc} and I_{sc} are the voltage and current over the short-circuit resistance R_{sc}, respectively, and U_{r} and I_{r} are the voltage and current over the load R_{r}, correspondingly. The inner phase of the cable is composed of a copper stabilizer with resistance R_{core}, which is connected in parallel to the resistances in the REBCO tape, i.e. the high-temperature superconductor R_{hts} and the resistance R_{aghycu}, which is equivalent to the resistances in parallel of copper R_{cu}, silver R_{ag} and Hastelloy® R_{hy}. *CB* is the circuit breaker.

3.4. Cable behavior in the case of a short circuit

Safe cable operation must be guaranteed, even in the case of short circuits. To simulate the current, voltage, resistance, and temperature of each cable material in the case of a fault, we developed an adiabatic 0D Python-coded cable model based on the circuit presented in figure 8. The circuit shows the inner (+) and outer (−) phases of one of the two monopoles selected for the cable topology (see section 3.1). During the rated operation, we assume that the current I_{r} flows through a load R_{r} equivalent to $U_0\, I_0^{-1}$. In the case of a short circuit, a current I_{sc} flows through a load R_{sc} that is much smaller than load R_{r}. We consider a short circuit that occurs at the end of the monopole.

When a short circuit occurs, a circuit breaker disconnects the cable from the electric grid within a certain latency time. According to the current profile I from a converter manufacturer, it takes less than 50 ms until the circuit breaker reacts. During this time, we estimate that the cable must withstand seven times more current than the minimum critical current $I_{\text{c,min}}$, that is, I_{max} is equal to 175 kA. This estimate is based on private communication with a manufacturer of superconducting cable terminations, after considering a current increase of approximately five to ten times the minimum critical current in accordance with [98].

The copper layers in the inner and outer phases are used to stabilize the cable electrically during the short circuit, because the amount of superconductor is determined to transmit the current $I_{\text{c,min}}$ only. The goal of the simulation is to determine an appropriate cross-section of the copper stabilizer A_{cu},

which can transmit excess current until the circuit breaker disconnects the cable. The copper cross-section A_{cu} will be the same for the inner and outer phases.

The purity of copper is often characterized by its residual resistivity ratio (RRR) [99]. This is the ratio of the resistivity at 293 K to that at 4.2 K. The RRR value of commercially pure copper wires ranges from 50 to 500 [99]. As a conservative assumption and aiming at low material costs, we assume the RRR to be 50. It should be noted that copper is generally resistant to hydrogen embrittlement, except when it contains oxygen or copper oxide [100].

For the inner phase, we consider a stranded copper wire with a fill factor f, meaning that

$$A_{cu} = f \cdot \pi \cdot r_{1,cu}^2. \tag{8}$$

A fill factor f of 60 % is common for stranded wires with high power density [101]. A stranded wire in the core provides flexibility and sufficient volume to wind the required number of REBCO tapes, while only a fraction f of copper is needed.

For the outer phase, we assume a wire made of solid drawn copper tape with the same height as the REBCO tape. Since the cross-section A_{cu} is the same for both the inner and outer phases, the radius of the outer copper stabilizer $r_{2,cu}$ is determined by

$$\pi \cdot r_{2,cu}^2 = \pi \cdot r_{2,hts}^2 + A_{cu}. \tag{9}$$

Solid drawn copper tapes allow flexibility, a smaller cable volume, and a lower surface roughness compared to a stranded wire in contact with liquid hydrogen inside the pipe.

The amount of electrical current flowing through each material in the cable depends on the respective electrical resistivity ρ. In appendix B, figure B.1 shows the assumed resistivities for copper, silver, Hastelloy®, and yttrium barium copper oxide (YBCO)–the assumed REBCO type–as a function of temperature. We assume that the critical temperature T_c of YBCO is 95 K. Below 95 K, the differential resistivity of YBCO is described by rephrasing the E–J power law [102] as:

$$\begin{aligned}\rho_{hts}(T_{cable}) &= \frac{E}{J_{hts}(T_{cable})} \\ &= \frac{E_c}{J_{hts}}\left(\frac{J_{hts}}{J_c(T_{cable})}\right)^n, (T_{cable}) < 95\text{K}.\end{aligned} \tag{10}$$

Here, J_{hts} is the current density of the superconductor, J_c is the critical current density dependent on the cable temperature T_{cable}, n is the power-law exponent, and E_c is the electric field criterion for J_c. We assume that the electric field criterion E_c is 1 μV cm^{-1} and the power-law exponent n is 30. In the flux flow regime, the electric field criterion E_c is assumed as 1 mV cm^{-1} and the power-law exponent n as 4.

Equation (10) shows that the differential resistivity of the HTS material is dependent on the electric current density. Therefore, the current flowing through it must be calculated at each time step. In addition, the critical current density depends on the cable temperature T_{cable}. Hence, the temperature of the superconducting material must also be continuously updated. Since we consider an adiabatic case, the temperature increase in time t can be calculated as [102]:

$$C_{cable}\frac{dT_{cable}}{dt} = P_{cable}, \tag{11}$$

$$\begin{aligned}C_{cable} &= C_{core} + C_{hts} + C_{aghycu}, \\ &= c_{core} \cdot V_{core} \cdot d_{core} + c_{hts} \cdot V_{hts} \cdot d_{hts} \\ &\quad + c_{aghycu} \cdot V_{aghycu} \cdot d_{aghycu},\end{aligned} \tag{12}$$

$$\begin{aligned}P_{cable} &= P_{core} + P_{hts} + P_{aghycu}, \\ &= R_{core} \cdot I_{core}^2 + R_{hts} \cdot I_{hts}^2 + R_{aghycu} \cdot I_{aghycu}^2,\end{aligned} \tag{13}$$

where C_{cable}, C_{core}, C_{hts}, and C_{aghycu} are the heat capacities of the cable, the copper stabilizer, the HTS material, and the remaining materials in the tape (Cu, Ag, and Hastelloy®), respectively, and P_{cable}, P_{core}, P_{hts}, and P_{aghycu} are the Joule heating losses of the cable, the copper stabilizer, the HTS material, and the remaining materials in the tape, respectively. The following variables are related to the copper stabilizer, the HTS material, and the remaining materials in the tape, respectively: c_{core}, c_{hts}, and c_{aghycu} are the temperature-dependent specific heat capacities (see figure B.2 of appendix B), V_{core}, V_{hts}, and V_{aghycu} are the volumes along the total length of 75 km, d_{core}, d_{hts}, and d_{aghycu} are the mass densities (see table B.1 of appendix B), R_{core}, R_{hts}, and R_{aghycu} are the resistances, and I_{core}, I_{hts}, and I_{aghycu} are the currents in the corresponding component.

To simulate the non-linear behavior of the HTS material, we use the two-branches model and the current-iterative process, as presented by [102]. Equation (11) can be solved numerically using the explicit Euler method [103]. For the calculation of the self-field critical current density, we use the fitted curves presented in figures A.2 and A.3 of appendix A. Since we consider a short circuit that occurs at the end of the transmission line (see figure 8), we assume a start temperature T_0 that corresponds to the outlet temperature of the liquid hydrogen. This is 26 K, which is one of the highest outlet temperatures for low mass flows (see section 3.5).

The voltage changes in the cable can be analyzed by applying Kirchhoff's law to the circuit shown in figure 8 [104]. Therefore, the source voltage U is a function of time t described as:

$$\begin{aligned}U(t) &= L_{cable}\frac{dI(t)}{dt} + I(t) \cdot R_{cable}(T_{cable}) + I(t) / \left(\frac{1}{R_{sc}} + \frac{1}{R_r}\right), \\ &= U_L + U_{cable} + I(t) / \left(\frac{1}{R_{sc}} + \frac{1}{R_r}\right),\end{aligned} \tag{14}$$

where R_{cable} and T_{cable} are the resistance and temperature, respectively, along the 75 km long cable. The load R_r is equivalent to $U_0\, I_0^{-1}$ and R_{sc} is a short-circuit resistance much smaller than the load R_r, as discussed at the beginning of this section. The current profile I assumes the existence of a capacitance in the grid. Considering this capacity would have nearly no impact on the heating of the superconducting material, which is the focus of this section. Therefore, the capacitance has been neglected. In equation (14), the inductance of a

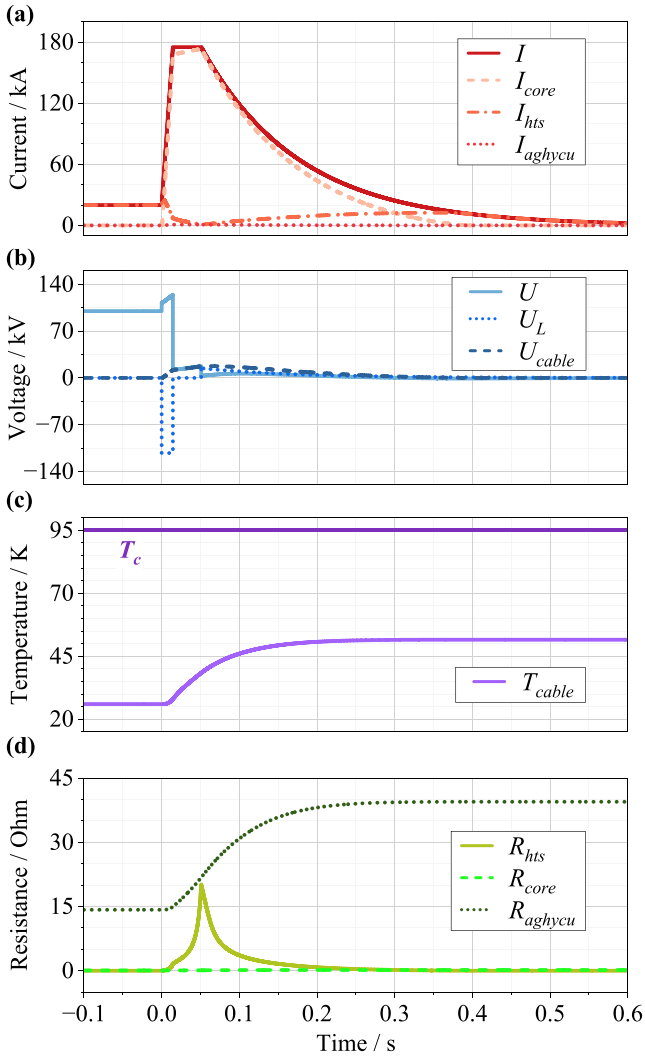

Figure 9. Cable behavior in the case of a short circuit: (a) Current changes in the current source I, in the copper core I_{core}, in the high-temperature superconductor (HTS) I_{hts} and in the rest of materials in the tape I_{aghycu} (silver, Hastelloy®, and copper); (b) Voltage fluctuations in the source U, in the inductance U_{L}, and in the cable U_{cable}; (c) Temperature rise in the cable T_{cable} accompanied by the critical current T_{c} of the HTS; (d) Resistance variations in the HTS R_{hts}, in the copper core R_{core}, and in the rest of materials in the tape R_{aghycu}.

coaxial cable L_{cable} is defined as:

$$L_{\text{cable}} = \frac{\mu_{\text{ins}} \cdot len}{2 \cdot \pi} \cdot \ln\left(\frac{r_{1,\text{ins}}}{r_{1,\text{hts}}}\right). \tag{15}$$

The permeability of the electric insulation μ_{ins} is equal to the relative permeability of a synthetic material μ_{rel} times the vacuum permeability μ_{o}, or rather $\mu_{\text{ins}} = \mu_{\text{rel}} \cdot \mu_{\text{o}}$. The relative permeability of the synthetic material is assumed to be 1.0.

Figure 9 illustrates the results of the cable simulation during the short circuit. The time stages can be described as follows: When the time t is less than 0.0 s, the cable is in rated operation. When time t equals 0.0 s, a short circuit occurs. Shortly thereafter, the peak current I_{max} is reached at 175 kA. When the time t is about 0.05 s, the circuit breaker activates and the source current I starts decreasing until it completely vanishes after approximately 0.6 s.

During the rated operation ($t < 0.0$ s), figure 9(a) shows that the entire source current I flows through the superconductor, such that the source current I is equal to the current through the superconductor I_{hts}. This is because the superconductor resistance R_{hts} vanishes during rated operation, as shown in figure 9(d). Even though the resistance of the inner copper stabilizer R_{core} is low, it is still five orders of magnitude higher than the superconductor resistance R_{hts}. In figure 9(d), the resistance R_{aghycu} represents the equivalent resistance of the other materials in the superconducting tape, as shown in figure 8. The resistance R_{aghycu} is considerably higher than the resistance of the superconductor R_{hts} and copper stabilizer R_{core}.

After the short circuit occurs at 0.0 s and until time t is approximately 0.3 s, the excess current is mainly transmitted by the inner copper stabilizer. This can be observed in figure 9(a), where the current through the copper stabilizer I_{core} is higher than the current through the superconductor I_{hts}. The current flow in the copper increases the cable temperature T_{cable}. This is illustrated in figure 9(c). The higher temperature significantly increases the resistance R_{aghycu}. The resistance of the copper stabilizer R_{core} rises slightly. The superconductor resistance R_{hts} increases sharply when the source current I is high. Despite a final temperature of approximately 51.6 K, the superconductor is able to transmit the remaining current starting from t equal to 0.3 s.

Figure 9(b) describes the changes in the source voltage U, cable voltage U_{cable}, and inductance voltage U_{L}–as described in equation (14). When a short circuit occurs, the inductance opposes the change in the electric current and a negative voltage is induced. This occurs during a sudden increase in the source current I. As soon as the source current I becomes constant at 175 kA, the inductance voltage U_{L} vanishes. Once the source current I decreases, the inductance voltage U_{L} becomes positive due to its opposing behavior. The inductance voltage U_{L} decreases as the source current I tends to zero. A maximum source voltage U_{max} of 124.4 kV is reached just before the source current I starts decreasing. This value is below the test voltage U_{T} of 185 kV, for which the cable should be designed, as discussed in section 3.2.

The results presented in figure 9 confirm the safe operation of the cable in the case of a short circuit from different perspectives. First, the cross-section of the copper stabilizer A_{core} is sufficiently large to transmit excess current during the short circuit. The radius of the copper stabilizer is also sufficient to wrap the necessary number of REBCO tapes for the rated operation. In principle, a slightly smaller copper stabilizer would also fulfill these two properties. However, the selected core copper radius $r_{1,\text{cu}}$ leads to an appropriate electric insulation thickness, as defined by equation (3). In addition, the resulting maximum voltage U_{max} is lower than the test voltage U_{T}. The voltage U_{max} is partly defined by the cable geometry, owing to its influence on the inductance, as shown in equations (14) and (15).

It should be noted that under the assumed adiabatic conditions, there is no heat exchange between the tape layers or

between the tape and the coolant liquid. The simulations conducted in [105] show that the difference in results between adiabatic and non-adiabatic simulations are negligible during a short circuit. This is because under fault conditions, rapid heat generation occurs within the tapes, and the coolant is unable to assist in reducing the temperature. However, after the short circuit, a non-adiabatic model can show how liquid hydrogen dissipates heat from the tapes. Therefore, the adopted adiabatic model is a worst-case scenario when modeling the temperature rise of the cable during a fault. In a non-adiabatic simulation, the final temperature of the cable would be even smaller.

The 0D simulation does not resolve the spatial dimensions, but focuses on the time-dependent behavior of the cable. In the 0D simulation, the cable temperature increases uniformly along the total length. According to [105], a 1D or 2D model can more precisely predict the risk of coolant warming as a consequence of an electric fault. However, an approximate heat transfer calculation can prove that the presented final temperature of about 51.6 K does not present a risk of coolant boiling. We consider a worst-case scenario, in which there is no coolant flow (constant volume), the amount of heat is totally transferred to the coolant, and the entire coolant is at the outlet temperature and pressure of approximately 26 K and 527 kPa, respectively (see section 3.5). The temperature difference between the coolant and the heated cable determines the amount of heat transferred, i.e. 630.8 MJ, given a cable heat capacity C_{cable} of 24 666 kJ K^{-1} at 51.6 K, as defined in equation (12). The density and specific heat capacity of liquid hydrogen at constant volume for the considered outlet temperature and pressure are about 63.2 kg m^{-3} and 6 117 J $kg^{-1}K^{-1}$, respectively [15]. Assuming the pipeline dimensions of the selected design that will be presented in the following section (15.8 cm^3 g^{-1}), the final coolant temperature and pressure would be of approximately 26.2 K and 671 kPa, respectively. Under these conditions, hydrogen remains in its liquid state and has still a safe distance to the vaporization curve (see section 3.5).

3.5. Thermal-hydraulic design

The main purpose of the thermal-hydraulic model is to calculate the temperature increase and pressure drop of liquid hydrogen along the pipeline length. We assume that sufficiently large storage tanks for liquid hydrogen are located at the beginning and at the end of the transmission line. On the upstream or supply side, the tank has liquid hydrogen in thermodynamic equilibrium at 150 kPa and 20.4 K. A transfer pump with an overhead pressure of 450 kPa provides an inlet pressure p_{in} of 600 kPA to the hybrid pipeline. According to an established manufacturer, such a transfer pump can be commercially designed to carry a mass flow of liquid hydrogen of up to 50 t h^{-1} or rather 13.9 kg s^{-1}. The equilibrium temperature in the container corresponds to the inlet temperature of the hybrid pipeline T_{in} of 20.4 K, as it is assumed that any temperature increase due to pressure rise is offset by heat transfer to the stored medium.

A Python-based simulation determines the outlet temperature T_{out} and outlet pressure p_{out} of the transmitted liquid hydrogen at the end of the pipeline. The numerical model is based on a simplified form of 1D compressible flow equations for the balance of mass, momentum and energy [106]. Since the pipeline length is much larger than its diameter, the differences in temperature and pressure between the beginning and end of the pipeline are given by [106]:

$$\bar{c}_{\text{p,LH2}} \cdot \frac{T_{\text{out}} - T_{\text{in}}}{len} = (1 - \bar{\alpha}_{\text{LH2}} \cdot \bar{T}) \cdot F + \frac{q}{\dot{m}_{\text{LH2}}}, \tag{16}$$

$$\frac{1}{\bar{\rho}_{\text{LH2}}} \cdot \frac{p_{\text{in}} - p_{\text{out}}}{len} = F + \frac{\bar{\alpha}_{\text{LH2}} \cdot \nu_{\text{LH2}}^2}{\bar{c}_{\text{p,LH2}}} \cdot \frac{q}{\dot{m}_{\text{LH2}}}, \tag{17}$$

$$F = \frac{\zeta}{D_{\text{h}}} \cdot \frac{\nu_{\text{LH2}}^2}{2}, \tag{18}$$

where T_{in}, T_{out}, p_{in}, and p_{out} are the corresponding inlet and outlet temperature and pressure, respectively, *len* is the pipeline length, $\bar{T}$ is the average value of the inlet and outlet temperature, q is the total heat load per unit length, F is correlated to the friction factor ζ, and D_{h} is the hydraulic diameter. The following variables are related to the transmitted liquid hydrogen: $\bar{c}_{\text{p,LH2}}$ is the average specific heat capacity at constant pressure, $\bar{\alpha}_{\text{LH2}}$ is the average thermal expansivity factor, $\dot{m}_{\text{LH2}}$ is the mass flow rate, ν_{LH2} is the flow speed, and $\bar{\rho}_{\text{LH2}}$ is the average mass density.

The assumptions made for the simplification of equations (16) and (17) are as follows:

- We assume that the slope between the starting and ending points is zero, because the altitude difference between Brunsbüttel and Hamburg is considerably small, especially close to the Elbe River.
- The Mach number is considered to be zero. This is because the ratio of the liquid-hydrogen flow speed–based on the hydrogen demand in Hamburg (see table 1)–to the speed of sound in liquid hydrogen is negligible [15, 106].

The following paragraphs introduce each of the variables in equations (16)–(18). The hydraulic diameter D_{h} is traditionally used as a basic approximation to consider arbitrary cross-sections as equivalent circular pipelines. Since the pipeline conducting liquid hydrogen contains two superconducting cables, the hydraulic diameter D_{h} is given by [107]:

$$D_{\text{h}} = \frac{4 \cdot A_{\text{pipe}}}{P_{\text{w}}} = \frac{2 \cdot \left(r_{\text{LH2,i}}^2 - 2 \cdot r_{\text{2,cu}}^2\right)}{r_{\text{LH2,i}} + 2 \cdot r_{\text{2,cu}}}, \tag{19}$$

$$A_{\text{pipe}} = \pi \cdot r_{\text{LH2,i}}^2 - 2 \cdot \pi \cdot r_{\text{2,cu}}^2, \tag{20}$$

$$P_{\text{w}} = 2 \cdot \pi \cdot r_{\text{LH2,i}} + 2 \cdot (2 \cdot \pi \cdot r_{\text{2,cu}}), \tag{21}$$

where $r_{\text{LH2,i}}$ is the inner radius of the tube carrying liquid hydrogen, $r_{\text{2,cu}}$ is the outer radius of each of the two superconducting cables situated inside, A_{pipe} is the effective flow cross-section, and P_{w} is the wetted perimeter (in contact with the fluid).

Despite the thermal insulation between the inner and outer pipelines, there is an unavoidable total heat load per unit length q on the inner pipe, which is determined by:

$$q = \lambda_0 + \lambda_{\text{cryo}} \cdot \pi \cdot D_{\text{LH2,i}}. \tag{22}$$

Here, λ_{cryo} is the specific heat output and λ_0 is a diameter-independent offset [85]. The reference surface is the cylindrical jacket of the pipe carrying liquid hydrogen with inner diameter $D_{\text{LH2,i}}$. Clearly, the heat load q increases linearly with the increasing diameter of the inner pipe.

To quantify the specific heat output λ_{cryo} and diameter-independent offset λ_0, several references were considered. First, the data provided in [108] considers vacuum jacketed pipes carrying liquid hydrogen. These data were linearly fitted, and the correlation was determined with a specific heat output λ_{cryo} equal to 3.3 W m^{-2} and diameter-independent offset λ_0 equal to 0.25 W m^{-1}, as shown in figure C.1 of appendix C. Second, according to [85], the combination of vacuum and 30 layers of multi-layer insulation creates a specific heat output λ_{cryo} of 1.2 W m^{-2} from 300 K to 21 K. The term for the diameter-independent offset λ_0 is neglected here, as it is considered to be related to electromagnetic losses that are less dominant under DC conditions. Third, both [53] and [52] set the heat load per unit length q to 2.0 W m^{-1}. In [53], the inner diameters under consideration are 12.6 cm and 15.2 cm. The authors in [52] analyze inner diameters up to 19.8 cm. This translates in a specific heat output λ_{cryo} of 3.2 W m^{-2} to 5.0 W m^{-2}, if the diameter-independent offset λ_0 is zero in equation (22) and if diameters larger than or equal to 12.6 cm are considered. We opted for an average value of the specific heat output λ_{cryo} of 3.2 W m^{-2} and a diameter-independent offset λ_0 of 0.25 W m^{-1}.

At the beginning and the end of the hybrid pipeline, additional thermal losses occur owing to the transition between the low and the ambient temperature of the current leads and cryostat terminations. Conventional, bath cooled current leads produce a minimum parasitic load of approximately 42 W kA^{-1} per pole at the transition between 300 K and 77 K, when using liquid nitrogen at an intermediate cooling step [109]. Superconducting current leads can produce, for example, a significantly lower heat load of approximately 3 W at 20 kA between 60 K and 4.5 K at the cold side [110]. Assuming the use of a superconducting current lead, plus a load-independent thermal loss of 20 W owing to the cryostat terminations (empirical value) [87], the thermal losses at the ends of the liquid hydrogen pipeline have been neglected because of the very small temperature difference given by the minimum mass flow requirements $\dot{m}_{\text{LH2}}$ of about 5.13 kg s^{-1} (see table 1).

The friction factor ζ on the liquid-hydrogen flow is calculated applying the Newton–Raphson method on the Colebrook–White implicit equation:

$$\frac{1}{\sqrt{\zeta}} = -2 \cdot \log\left(\frac{\epsilon}{3.7 \cdot D_{\text{h}}} + \frac{2.51}{Re\sqrt{\zeta}}\right), \tag{23}$$

where ϵ is the surface roughness, D_{h} is the hydraulic diameter and Re is the Reynolds number. It has been shown that the hydraulic diameter D_{h} can be used to calculate the friction factor for turbulent flows ($Re > 4\,000$) in non-circular cross-sections if there are no sharp edges inside [107]. A more detailed determination of the friction factor for the presented geometry is beyond the boundaries of this work.

The liquid hydrogen is mainly transmitted between two materials: copper and invar. Therefore, the surface roughness ϵ of the outer copper layer of the cable and of the inner invar pipe must be considered. According to [111, 112], and [113], the surface roughness ϵ is equal to 0.046 mm for commercial steel pipes, which is the most similar value found in the literature for invar. In the case of drawn copper, the surface roughness ϵ is equal to 0.0015 mm [111]. As a conservative approach, the surface roughness ϵ is assumed to be equal to 0.046 mm for the simulation.

The Reynolds number Re in equation (23) is defined as:

$$Re = \frac{\nu_{\text{LH2}} \cdot D_{\text{h}} \cdot \bar{\rho}_{\text{LH2}}}{\bar{\eta}_{\text{LH2}}}, \nu_{\text{LH2}} = \frac{\dot{m}_{\text{LH2}}}{\bar{\rho}_{\text{LH2}} \cdot A_{\text{pipe}}}, \tag{24}$$

where $\bar{\eta}_{\text{LH2}}$ is the average viscosity associated with the liquid hydrogen flow. The mean values of the mass density $\bar{\rho}_{\text{LH2}}$, specific heat capacity $\bar{c}_{\text{p,LH2}}$, thermal expansivity factor $\bar{\alpha}_{\text{LH2}}$, and viscosity $\bar{\eta}_{\text{LH2}}$ in equations (16)–(24) are calculated based on the substance data for parahydrogen from [15], using the average values of the assumed inlet and outlet temperatures and pressure, that is, $\bar{\rho}_{\text{LH2}}(\bar{T},\bar{p})$, $\bar{c}_{\text{p,LH2}}(\bar{T},\bar{p})$, $\bar{\alpha}_{\text{LH2}}(\bar{T},\bar{p})$, and $\bar{\eta}_{\text{LH2}}(\bar{T},\bar{p})$, where

$$\bar{T} = \frac{T_{\text{in}} + T_{\text{out}}}{2}, \bar{p} = \frac{p_{\text{in}} + p_{\text{out}}}{2}. \tag{25}$$

To initialize the values of the average temperature $\bar{T}$ and average pressure $\bar{p}$, an initial value of the outlet pressure p_{out} is adopted by establishing a maximum difference between the outlet pressure p_{out} and the inlet pressure p_{in}, for example, of 300 kPa. The initial value of the outlet pressure p_{out} is used to calculate the saturation temperature T_{sat} of liquid hydrogen at the given pressure. We assume that the maximum outlet temperature T_{out} of the liquid hydrogen must be at least 1K away from the boiling curve, that is,

$$T_{\text{out}} \leq T_{\text{sat}}(p_{\text{out}}) - 1\ \text{K}. \tag{26}$$

This condition stipulates the safety margin for the boiling curve. Using the initial values of the outlet temperature T_{out} and outlet pressure p_{out}, we use equation (25) to calculate the mean mass density $\bar{\rho}_{\text{LH2}}$, mean specific heat $\bar{c}_{\text{p,LH2}}$, mean thermal expansivity factor $\bar{\alpha}_{\text{LH2}}$, and mean viscosity $\bar{\eta}_{\text{LH2}}$. These values are used in equations (24)–(17) to determine the self-consistent values of the outlet temperature T_{out} and pressure p_{out} as a function of the mass flow $\dot{m}_{\text{LH2}}$, and the pipe inner diameter $D_{\text{LH2,i}}$. The calculation usually converges after approximately five iterations, with a relative change in the outlet temperature T_{out} and pressure p_{out} of 10^{-7} as the convergence criterion. Table 4 presents an example of the parameter values for the case when the pipe inner diameter $D_{\text{LH2,I}}$ is equal to 36 cm and the mass flow $\dot{m}_{\text{LH2}}$ is equal to 6.0 kg s^{-1}.

Figure 10 illustrates the results of the thermal-hydraulic simulation. Figure 10(a) presents the outlet temperature T_{out}

Table 4. Example of parameter values in the thermal-hydraulic simulation when the pipe inner diameter $D_{\mathrm{LH2,i}}$ and the mass flow $\dot{m}_{\mathrm{LH2}}$ are set to 36 cm and 6.0 kg s^{-1}, respectively.

Parameter	Value
T_{in}	20.4 K
p_{in}	600.0 kPa
λ_{cryo}	3.2 W m^{-2}
λ_0	0.25 W m^{-1}
q	3.857 W m^{-1}
ϵ	0.046 mm
$D_{\mathrm{LH2,i}}$	36.0 cm
D_{h}	25.2 cm
A_{pipe}	957.9 cm^2
P_{w}	151.9 cm
$\dot{m}_{\mathrm{LH2}}$	60.0 kg s^{-1}
$\bar{T}$	22.6 K
$\bar{p}$	539.4 kPa
$\bar{\rho}_{\mathrm{LH2}}$	68.5 kg m^3
$\bar{c}_{\mathrm{p,LH2}}$	11 044.4 J kg^{-1} K^{-1}
$\bar{\alpha}_{\mathrm{LH2}}$	0.0196 K^{-1}
$\bar{\eta}_{\mathrm{LH2}}$	11.54 µPa s
ν_{LH2}	0.914 m s^{-1}
Re	1 368 309
ζ	0.0142
T_{out}	24.9 K
p_{out}	478.7 kPa

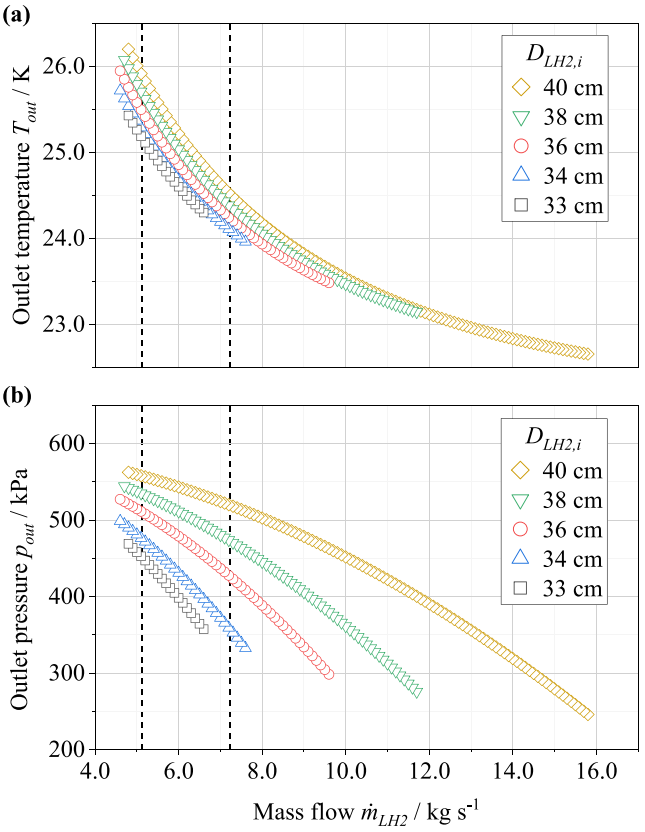

Figure 10. (a) Outlet temperature T_{out} and (b) outlet pressure p_{out} of the hybrid pipeline, both as a function of the mass flow of liquid hydrogen $\dot{m}_{\mathrm{LH2}}$. The results are presented for four different inner diameters $D_{\mathrm{LH2,i}}$ of the pipe carrying the liquid hydrogen: 33 cm, 34 cm, 36 cm, 38 cm, and 40 cm. The vertical dashed lines show the limits of the hydrogen demand in the selected case study: between 5.13 kg s^{-1} (0.61 GW$_{\mathrm{t}}$) and 7.23 kg s^{-1} (0.86 GW$_{\mathrm{t}}$). For the design, we selected $D_{\mathrm{LH2,i}}$ of 36 cm.

and figure 10(b) shows the outlet pressure p_{out}, both in terms of the dependency on the mass flow $\dot{m}_{\mathrm{LH2}}$. Each figure compares five different inner pipe diameters $D_{\mathrm{LH2,i}}$: 33 cm, 34 cm, 36 cm, 38 cm, and 40 cm. The condition based on equation (26) indicates that for the presented results, hydrogen will remain in its liquid state–even after 75 km of transmission and without the need for intermediate cooling stations. The smallest integer value for the diameter required to fulfill this condition is 33 cm. Diameters larger than 40 cm are also appropriate; however, they require higher ranges of mass flow $\dot{m}_{\mathrm{LH2}}$, as it will be discussed as follows.

The results show several effects of different pipe inner diameters $D_{\mathrm{LH2,i}}$ and mass flows $\dot{m}_{\mathrm{LH2}}$ on the outlet temperature T_{out} and pressure p_{out}. For a given mass flow $\dot{m}_{\mathrm{LH2}}$, the outlet temperature T_{out} is higher for larger values of diameter $D_{\mathrm{LH2,i}}$. This is expected because of a higher heat load q, as described by equation (22). Since the cryogenic losses are smaller for smaller pipe diameters, lower values of the flow speed ν_{LH2} -and hence of the mass flow $\dot{m}_{\mathrm{LH2}}$ -are allowed for smaller diameters $D_{\mathrm{LH2,i}}$. However, small pipe diameters increase the frictional losses. Therefore, higher operational values of the mass flow $\dot{m}_{\mathrm{LH2}}$ can be achieved by pipes with larger diameters $D_{\mathrm{LH2,i}}$, as described by equations (16) and (17). For all diameters $D_{\mathrm{LH2,i}}$, figure 10(b) shows that if the mass flow $\dot{m}_{\mathrm{LH2}}$ is higher, the outlet pressure p_{out} will be lower, mainly because of the higher frictional losses. In contrast, figure 10(a) shows that for higher values of the mass flow $\dot{m}_{\mathrm{LH2}}$, the outlet temperature T_{out} will be lower–according to equation (16)–since the liquid hydrogen will be transmitted faster. At low mass flows $\dot{m}_{\mathrm{LH2}}$, the opposite occurs, that is, the pressure drop is lower because the frictional losses are smaller, and the temperature difference is higher because the velocity ν_{LH2} is lower.

To choose an appropriate diameter $D_{\mathrm{LH2,i}}$ for our design, the vertical dashed lines in figure 10 represent the limits of the hydrogen demand for the selected case study. According to table 1, the minimum hydrogen demand will be 5.13 kg s^{-1} (0.61 GW$_{\mathrm{t}}$) and the maximum hydrogen demand will be 7.23 kg s^{-1} (0.86 GW$_{\mathrm{t}}$). On one hand, the hybrid pipeline should be in operation even though hydrogen quantities lower than the minimum demand are available. The lowest values of $\dot{m}_{\mathrm{LH2}}$ of 4.6 kg s^{-1} (0.55 GW$_{\mathrm{t}}$) are achieved when the inner diameter $D_{\mathrm{LH2,i}}$ is 34 cm or 36 cm. On the other hand, if the hydrogen demand in Hamburg grows in the future, the diameter $D_{\mathrm{LH2,i}}$ of 36 cm permits a mass flow $\dot{m}_{\mathrm{LH2}}$ as high as 9.6 kg s^{-1} (1.14 GW$_{\mathrm{t}}$), compared to only 7.6 kg s^{-1} (0.91 GW$_{\mathrm{t}}$) with a diameter of 34 cm, in return for a modest diameter enlargement. For these reasons, we select an inner diameter $D_{\mathrm{LH2,i}}$ equal to 36 cm. The operational range is defined by the design parameter values listed in table 5.

Figure 11 shows the density of liquid hydrogen as a function of both the temperature and pressure in the relevant range of operation of the hybrid pipeline [15]. The white curve

Table 5. Thermal-hydraulic design parameters and corresponding range of operation.

Parameter	Value
T_{in}	20.4 K
p_{in}	600.0 kPa
q	3.857 W m^{-1}
ϵ	0.046 mm
$D_{LH2,i}$	36.0 cm
$\dot{m}_{LH2}$	4.6 – 9.6 kg s^{-1} 0.55 – 1.14 GW$_t$
T_{out}	25.9 – 23.5 K
p_{out}	527.1 – 298.3 kPa

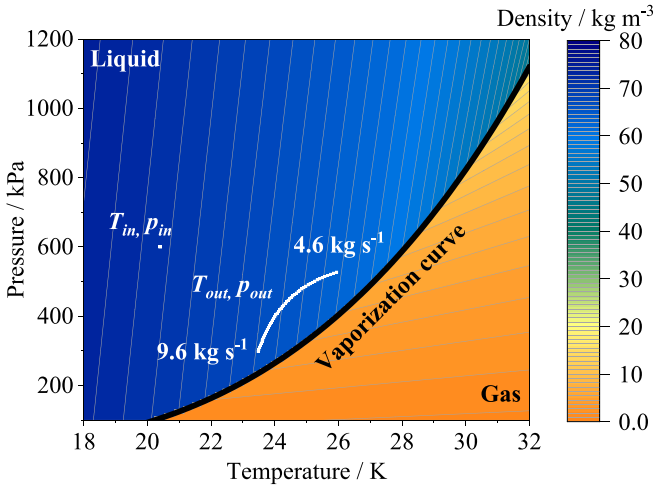

Figure 11. Density of liquid hydrogen as a function of pressure and temperature in the relevant range of operation of the hybrid pipeline, based on data from [15]. The dark curve is the phase boundary between gas and liquid state. T_{in} and p_{in} are the inlet temperature and inlet pressure, correspondingly. T_{out} and p_{out} are the calculated outlet temperature and outlet pressure, respectively, considering mass flows $\dot{m}_{LH2}$ from 4.6 kg s^{-1} and 9.6 kg s^{-1} for the selected inner diameter $D_{LH2,i}$ of 36 cm.

presents the calculated values of the outlet temperature T_{out} and pressure p_{out} at a given mass flow $\dot{m}_{LH2}$ between 4.6 kg s^{-1} and 9.6 kg s^{-1} for the selected diameter $D_{LH2,i}$ of 36 cm. The dark curve represents the phase boundary between the gas and liquid states. The white dot (T_{in}, p_{in}) represents the inlet parameters. Figure 11 shows that liquid hydrogen is a compressible fluid. The thermal expansivity factor $\bar{\alpha}_{LH2}$ acknowledges this fact in equations (16) and (17) [106]. The inlet density falls from approximately 71.3 kg m^{-3} to 63.6 kg m^{-3} in the outlet, when $\dot{m}_{LH2}$ is equal to 4.6 kg s^{-1}. This is a density difference of approximately 11.2%. In the case of a mass flow $\dot{m}_{LH2}$ equal to 9.6 kg s^{-1}, the density decreases to approximately 66.9 kg m^{-3}. This corresponds to a reduction of approximately 6.2%.

To calculate the wall thicknesses of the inner and outer pipes, the materials and pressures involved must be considered. The inner pipe must stand at an inlet pressure p_{in} of 600 kPa on the inner side, and a pressure close to vacuum on the outer side. As a safety measure, we assume that the inner pipe must hold PN 16 or a nominal pressure of 1600 kPa. The inner pipe wall thickness–given by the difference between the radii $r_{LH2,o}$ and $r_{LH2,i}$ -was based on the standards for pressure equipment AD 2000 and is equal to 5 mm. Since invar is not listed in the AD 2000 for hydrogen and low-temperature applications, an individual assessment is necessary.

Table 6. Radii of the inner and outer pipes for the selected inner diameter $D_{LH2,i}$, where $r_{LH2,o}$ and $r_{LH2,i}$ are the outer and inner radii of the liquid hydrogen conducting pipeline, respectively, and $r_{pipe,o}$ and $r_{pipe,i}$ are the outer and inner radii of the outer pipeline, correspondingly.

Parameter	Value
$r_{LH2,i}$	180.0 mm
$r_{LH2,o}$	185.0 mm
$r_{pipe,i}$	215.0 mm
$r_{pipe,o}$	224.0 mm

The space between the inner and outer pipes should be sufficient to include the multi-layer insulation–which reduces thermal losses by convection–and some free space to reduce the heat load by conduction. We propose a distance of 30 mm between the radii $r_{LH2,o}$ and $r_{pipe,i}$, such that 20 mm is available for 40 layers of multi-layer insulation and 10 mm are available for free space. The thickness of the outer pipeline–given by the difference between the radii $r_{pipe,o}$ and $r_{pipe,i}$ -is based on the conservative design guideline 1/50 wall thickness to diameter ratio for long vacuum pipes of carbon steel [114]. Table 6 summarizes the radii of the inner and outer pipes, and their corresponding thicknesses.

The thermal-hydraulic model showed how to conserve hydrogen in its liquid state and proposed the pipeline thicknesses, but the presented approach has some limitations. The calculation of the inner diameter $D_{LH2,i}$ tends to be underestimated, because no curves, fittings, or support structures inside the inner pipeline were included in this analysis. It should be noted that this study does not investigate safety measures in the case of a fault that leads to liquid-hydrogen boiling. It is clear that emergency valves should be installed periodically along the hybrid pipeline to steam gaseous hydrogen in the case of excess pressure.

4. Discussion and outlook

The analysis in this work presents multiple reasons for using a hybrid pipeline between Brunsbüttel and Hamburg, in northern Germany. On the one hand, Brunsbüttel has become an interconnecting point for the import and transmission of both electrical energy and hydrogen, possibly in liquid state. On the other hand, Hamburg is a city that gathers many of the perspective uses of both energy vectors for decarbonization. This indicates that it is pertinent to take advantage of the synergetic transmission of a hybrid pipeline, for example, to reduce the space and energy requirements for energy transmission in bulk, but also to assure the efficient delivery of hydrogen in the liquid state.

The quantitative results demonstrate the efficient and compact transfer of both energy vectors. A 75 km long hybrid

pipeline with an outer diameter of less than 45 cm can transmit large amounts of energy. 4.0 GW_e of electrical energy and 0.55 GW_t to 1.14 GW_t of liquid hydrogen can be transmitted without the need of intermediate cooling stations. This corresponds to the delivery of 397 t d^{-1} to 829 t d^{-1} of liquid hydrogen.

The proposed hybrid pipeline exhibits the following technical benefits over conventional transmission alternatives. A high-voltage DC link, such as SuedLink, requires 18 m to 22 m width to transmit 4 GW_e [115]. A conventional 50 cm wide pipeline transmits 1.2 GW_t of gaseous hydrogen at an operating pressure of 5 000 kPa [116]. The hybrid pipeline in this case study requires an inlet pressure of only 600 kPa, which suggests a lower energy input for the overhead pressure. However, a comparison with conventional transmission alternatives requires a more extensive analysis that considers all components involved in the transmission. The next steps of our project will build on the design of this hybrid pipeline to evaluate its techno-economic competitiveness compared to conventional alternatives.

Earlier works with specific technical designs of hybrid pipelines have presented outcomes not considered in this paper. Trevisani demonstrated that the AC ripple losses caused by the power electronics converters can be neglected in comparison to the thermal losses through the cryostat [50]. Mimmi *et al* investigated three different magnesium diboride cable designs at ±25 kV (medium voltage) and 20 kA under various electro-thermal operational and fault conditions. The authors concluded that a multi-bundle petal configuration provides a higher number of magnesium diboride wires within a small diameter of 23.5 mm, and an acceptable magnetic field on the wires of about 0.65 T [55]. Yamada *et al* considered a 1 000 km long hybrid pipeline with an outer diameter of 22 cm that transmits 1 GW_e and 0.14 GW_t in form of liquid hydrogen. The considered transmission requires cryogenic refrigeration every 10 km with a total power consumption of 13.2% of the electrical transport capacity of 1 GW_e, when considering an inlet point of 17 K and 400 kPa, and a heat load of 1 W m^{-1} [51]. Using a liquid nitrogen cold shield, Fu *et al* determined that the maximum transmission distance of a hybrid pipeline, which transmits 0.15 GW_e and 0.08 GW_t of liquid hydrogen within an outer diameter of less than 17 cm, is 100 km without intermediate cooling stations [58].

Previous studies have also proved the use of hybrid pipelines along several tens of kilometers without intermediate cooling stations and cold shields. For example, transmission distances of 30 km and up to 120 km were simulated in [53] by Bracco *et al* and [52] by Savoldi *et al*, respectively. However, the transmission capacities and pipe diameters in these studies are smaller than in our design. In [53], a 30 km submarine hybrid pipeline is proposed for the transmission of 0.3 GW_e and at least $60-70$ MW_t of liquid hydrogen from an offshore wind farm to the coast. The considered inner diameters are 12.6 cm and 15.2 cm. The authors in [52] suggested a transmission capacity of 0.1 GW_e and >0.1 GW_t, at inlet pressures between 2 000 and 3 000 kPa, for inner diameters up to 19.8 cm. Both [53] and [52] set the heat load per unit length q to 2.0 W m^{-1}. This corresponds to a specific heat output λ_{cryo} of 3.2 W m^{-2} to 5.0 W m^{-2}, as discussed in section 3.5. In contrast, we assume a specific heat output λ_{cryo} of 3.2 W m^{-2}. This theoretical assumption should be verified in future research, as an experimental verification is out of the scope of this study.

5. Conclusion

This work has presented a compact and efficient design of a hybrid pipeline for the synergetic transmission of electrical energy and liquid hydrogen between Brunsbüttel and Hamburg, in northern Germany. For this purpose, the supply and demand of both energy vectors have been investigated. The conceptual design covered the electrical topology, cable build-up, behavior of the cable in the case of a short circuit, and thermal-hydraulic design. The main findings of this study are as follows:

1. *Large energy transmission with small space and material needs*: A pipe diameter of 44.8 cm is enough to transmit 4.0 GW_e of electrical energy and 0.55 GW_t to 1.14 GW_t of liquid hydrogen along 75 km. This is equivalent to a hydrogen flow between 397 t d^{-1} and 829 t d^{-1}. The proposed cable design has a rated voltage of ± 100.0 kV and a rated current of 20 kA.
2. *Secure operation, even in the case of a short circuit*: Two parallel coaxial monopoles with metallic return provide electrical redundancy, no magnetic field outside the cables and mechanical flexibility. The cables would withstand a fault with an overcurrent of 175 kA for 50 ms. The coolant would maintain in its liquid state despite of a cable temperature rise up to 51.6 K. The increase of pressure remains inside the design limits.
3. *Efficient liquid hydrogen transmission without intermediate cooling*: A 75 km long pipeline with an inner diameter of 36 cm transmits 4.6 kg s^{-1} to 9.6 kg s^{-1} of liquid hydrogen without evaporation. We consider an inlet pressure of 600 kPa, an inlet temperature of 20.4 K, a specific heat output equal to 3.2 W m^{-2}, and a diameter-independent offset equal to 0.24 W m^{-1}.
4. *Review of potential users of liquid hydrogen*: liquid hydrogen proves to be useful, not only for the import of hydrogen overseas, but also for the decarbonization of several types of consumers, including parts of the aviation and maritime sectors, as well as long-range trucks. This is mainly because of its high energy density. The high purity of liquid hydrogen makes it attractive to other final users, such as chip companies and fuel cells. The cryogenic temperature level of liquid hydrogen enables the use of HTSs, which can be used to expand the electric grid with low space and material requirements.

The present work has ascertained where and how a hybrid pipeline can synergetically transmit electrical energy and liquid hydrogen in Germany. However, a technology will only prevail if it is cost-competitive. Future steps in this project will deliver a techno-economic assessment of this hybrid pipeline compared with conventional transmission alternatives. The

results of this paper and future project steps will be available to relevant stakeholders and policy makers to take better-informed decisions when considering the expansion of transmission infrastructure to reach climate neutrality.

Data availability statement

The data are not available in a format that is sufficiently accessible or reusable by other researchers.

Acknowledgments

This work was funded by the German Federal Ministry of Research, Technology and Space as well as the European Union—NextGenerationEU (project name 'TransHyDE—project AppLHy!', funding Reference No. 03HY204A). The responsibility for the content lies with the authors and does not necessarily reflect the opinion of the project consortium.

The authors would like to thank Professor L Savoldi, Professor A Morandi, the manufacturer of superconducting cable terminations, the manufacturer of cryogenic transfer pumps, and the manufacturer of cryogenic pipelines for the very useful discussions.

Conflict of interest

The authors declare that they have no affiliations with or involvement in any organization or entity with any financial interest in the subject matter or materials discussed in this manuscript.

Author contributions

Sebastian Palacios 0000-0003-4145-6365
Conceptualization (equal), Data curation (lead), Formal analysis (lead), Investigation (lead), Visualization (lead), Writing – original draft (lead), Writing – review & editing (lead)

Michael J Wolf 0000-0001-9080-080X
Funding acquisition (supporting), Investigation (supporting), Supervision (supporting), Writing – review & editing (supporting)

Mathias Noe 0009-0006-5870-968X
Conceptualization (equal), Supervision (lead), Writing – review & editing (supporting)

Mira Wehr 0009-0008-1747-0339
Investigation (supporting)

Tabea Arndt 0000-0002-7797-8862
Conceptualization (equal), Funding acquisition (lead), Project administration (lead), Supervision (supporting), Writing – review & editing (supporting)

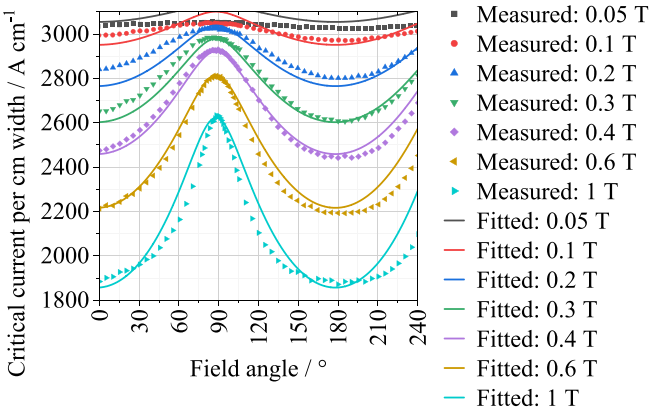

Figure A.1. Dependence of the critical current per cm width of the selected REBCO tape on field angle at 30 K. Different magnetic flux densities are presented as independent datasets. The measured data were fitted using an elliptical model as described in [103].

Appendix A. REBCO tape critical current measurements and fitted curves

REBCO probes of the chosen HTS producer were delivered to the Robinson Research Institute in New Zealand to measure the critical current. The critical current of the 1 mm wide short probes was measured at temperatures from 20 K to 77 K, magnetic flux densities from 0 T to 1 T, and angles from 0° to 240°. For design purposes, the measured data were fitted using various techniques. Here, we present the results.

The critical current per cm width is shown as a function of the field angle in figure A.1. Several curves show the effect of an increasing magnetic flux density. The continues lines next to the discrete measured values show how the data were fitted using an elliptical model, as described in [97]. It can be observed that the critical current has lower values at 0° and 180° and a maximum at 90°. As expected, the critical current decreases when the magnetic flux density is higher.

Figure A.2 presents the critical current per cm width as a function of temperature. We determine the field angle to be the one that induces the lowest critical current as a conservative assumption. We assume that the critical temperature of the HTS is 95 K. The thin plate spline method was used to fit the sample data. Here, the different curves show also the effect caused by an increasing magnetic flux density. It is clear that the higher the temperature the lower the critical current.

Figure A.3 shows the effect of the magnetic flux density on the critical current per centimeter width. The multiple datasets represent a discrete change of temperature. Here, the field angle is fixed to produce the lowest critical current. This assumption is conservative. The fitting method used was a thin-plate spline. As expected, the critical current decreases with an increase of both temperature and magnetic flux density.

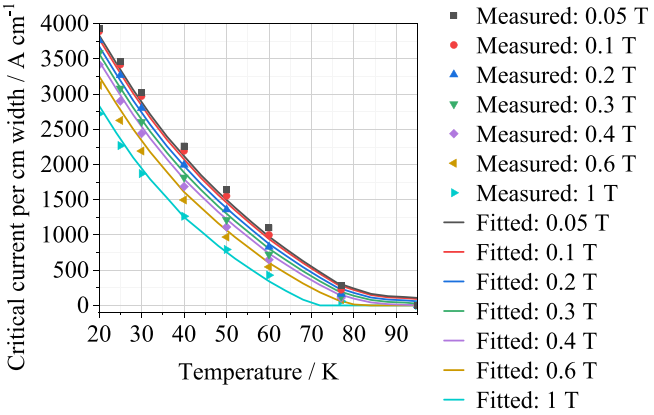

Figure A.2. Critical current per cm width of the selected REBCO tape as a function of temperature at the field angle with the minimum critical current. The critical temperature is assumed to be 95 K. Different magnetic flux densities are presented as independent datasets. The thin plate spline method was used to fit the sample data.

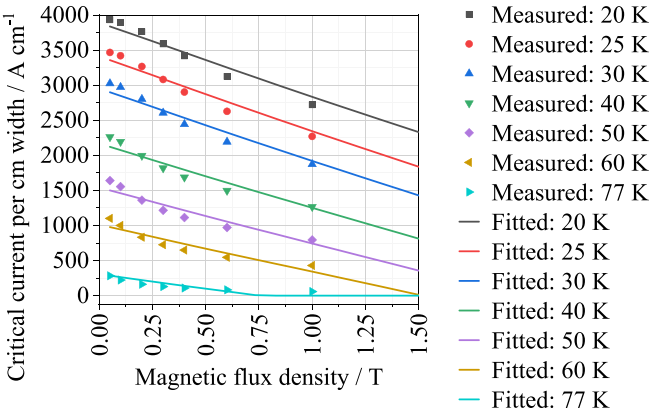

Figure A.3. Measurements and fitted curves of the critical current per cm width of the selected REBCO tape depending on the magnetic flux density at the field angle with the minimum critical current. Different temperatures are presented as independent datasets. The thin plate spline method was used to fit the sample data.

Appendix B. Resistivities, specific heat capacities, and mass densities of the materials in the cable

This section summarizes the material properties used for the model of the short-circuit behavior of the cable. Figure (B.1a) illustrates the assumed resistivities for copper [99], silver [117], and Hastelloy® [118] as a function of the temperature between 10 and 300 K. For YBCO, the assumed resistivity is presented from 95 to 300 K in figure (B.1b) [119]. We assume that the critical temperature of YBCO is 95 K. Below this temperature, the resistivity of YBCO is described using power law (see section 3.4).

To simulate the temperature variation in each component of the cable, we utilize the specific heat capacities of copper, silver, Hastelloy®, and YBCO, which are temperature-dependent and referenced from [117, 118, 120], and [121] respectively, as

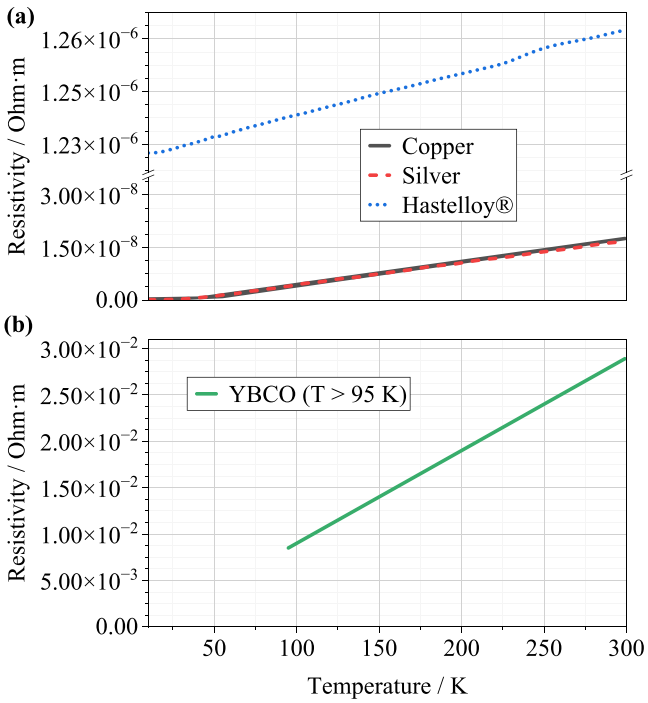

Figure B.1. (a) Resistivity of copper, silver, and Hastelloy® from 10 K to 300 K based on [99, 117], and [118]. (b) Resistivity of YBCO from 95 K to 300 K based on [119]. Below the critical temperature of 95 K, the resistivity of YBCO is described using power law.

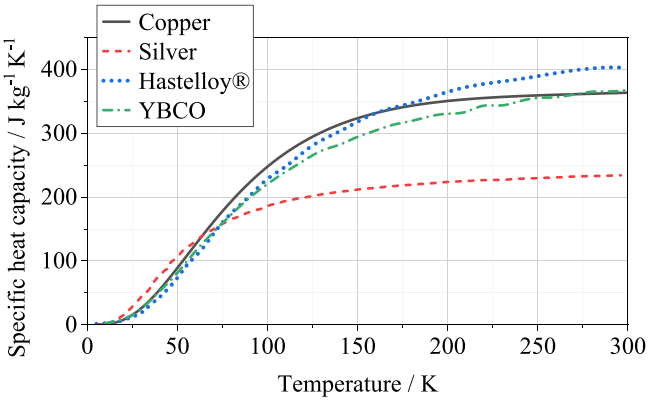

Figure B.2. Specific heat capacities of copper, silver, Hastelloy® and YBCO based on [117, 118, 120], and [121].

Table B.1. Mass densities of the modeled materials in the cable.

Material	Density
Copper	8 940 kg m^{-3} [122]
Silver	10 492 kg m^{-3} [117]
YBCO	6 380 kg m^{-3} [123]
Hastelloy®	8 890 kg m^{-3} [118]

illustrated in figure B.2. Subsequently, the specific heat capacity is multiplied by the volume and mass density of each material. Table B.1 lists the assumed mass densities.

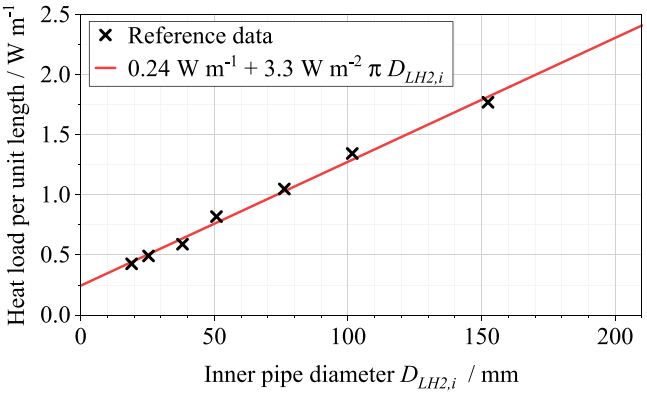

Figure C.1. Heat load per unit length as a function of the inner pipe diameter for a vacuum jacketed liquid hydrogen pipeline based on reference data from [108]. The data was linearly fitted and the correlation is shown a continuous line.

Appendix C. Reference data for heat load on a liquid hydrogen pipeline

The sample data from [108] were linearly fitted to establish the total heat load per unit length of vacuum-jacketed pipes carrying liquid hydrogen. The correlation was defined with a specific heat output of 3.3 W m^{-2} and a diameter-independent offset of 0.24 W m^{-1}, as shown in figure C.1. Here, $D_{\mathrm{LH2,i}}$ is the inner diameter of the considered pipeline.

References

[1] Bundestag 2019 *Bundes-Klimaschutzgesetz: KSG*

[2] Stiftung Klimaneutralität 2022 Vergleich der „Big 5“ Klimaneutralitätsszenarien (available at: www.stiftung-klima.de/app/uploads/2022/03/2022-03-16-Big5_Szenarienvergleich_final.pdf) (Accessed 4 December 2025)

[3] Fraunhofer Institut für System- und Innovationsforschung (Fraunhofer ISI), Consentec. GmbH, ifeu and TU Berlin 2022 *Langfristszenarien für die Transformation des Energiesystems in Deutschland: Treibhausgasneutrale Szenarien T45*

[4] Bundesverband der Energie- und Wasserwirtschaft e.V (BDEW) 2023 *Die Energieversorgung 2023 – Jahresbericht –*

[5] Agora Think Tanks 2024 *Klimaneutrales Deutschland: Von der Zielsetzung zur Umsetzung*

[6] Bundesnetzagentur 2024 *Netzausbau Strom: Bedarfsermittlung 2023–2037/2045: Bestätigung Netzentwicklungsplan Strom*

[7] Vereinigung der Fernleitungsbetreiber Gas e.V 2024 *Netzentwicklungsplan Gas 2022–2032*

[8] Bundesministerium für Justiz 2024 *Gesetz zur Entwicklung und Förderung der Windenergie auf See: Windenergie-auf-See-Gesetz—WindSeeG*

[9] The Federal Government 2024 *Import Strategy for Hydrogen and Hydrogen Derivatives* (Federal Ministry for Economic Affairs and Energy)

[10] Agora Energiewende, Agora Industrie and Guidehouse 2024 *Wasserstoffimporte Deutschlands—Welchen Beitrag können Pipelineimporte in den 2030er Jahren leisten?*

[11] Hank C *et al* 2023 *Power-To-X Country Analyses—Site-Specific, Comparative Analysis for Suitable Power-to-X Pathways and Products in Developing and Emerging Countries: A Cost Analysis Study on Behalf of H2Global* (Fraunhofer-Institut für Solare Energiesysteme ISE (Fraunhofer ISE))

[12] Pieton N *et al* 2024 *In-Depth Techno-Economic Assessment of Hydrogen and PtX Export Supply Chains: HYPAT Working Document* (Fraunhofer-Einrichtung für Energieinfrastrukturen und Geothermie IEG (Fraunhofer IEG))

[13] Staiß F *et al* 2022 *Options for Importing Green Hydrogen into Germany between Now and 2030 (Materials)* (Schriftenreihe Energiesysteme der Zukunft)

[14] Zhang F, Zhao P, Niu M and Maddy J 2016 The survey of key technologies in hydrogen energy storage *Int. J. Hydrog. Energy* **41** 14535–52

[15] Huber M, Harvey A, Lemmon E, Hardin G, Bell I and McLinden M 2018 *Reference Fluid Thermodynamic and Transport Properties (REFPROP) Version 10.0—SRD 23* (National Institute of Standards and Technology (NIST))

[16] The Compressed Gas Association, Inc. 2024 *CGA G-5.3-2024—Commodity Specification for Hydrogen* 8th edn (available at: https://webstore.ansi.org/standards/cga/cga2024-2548518) (Accessed 4 December 2025)

[17] Pacific Northwest National Laboratory 2023 H2tools *Hydrogen Tools: What is the Hydrogen Purity Requirement for Hydrogen?* (available at: https://h2tools.org/faq/hydrogen-purity-requirements) (Accessed 4 December 2025)

[18] Tiwari S, Pekris M J and Doherty J J 2024 A review of liquid hydrogen aircraft and propulsion technologies *Int. J. Hydrog. Energy* **57** 1174–96

[19] Laursen R *et al* 2023 *Potential of Hydrogen as Fuel for Shipping* (European Maritime Safety Agency)

[20] Ahluwalia R K *et al* 2023 Liquid hydrogen storage system for heavy duty trucks: configuration, performance, cost, and safety *Int. J. Hydrog. Energy* **48** 13308–23

[21] Miyazaki J, Kajiyama T, Matsumoto K, Fujiwara H and Yatabe M 1996 Ultra high purity hydrogen gas supply system with liquid hydrogen *Int. J. Hydrog. Energy* **21** 335–41

[22] Zhao Y, Mao Y, Zhang W, Tang Y and Wang P 2020 Reviews on the effects of contaminations and research methodologies for PEMFC *Int. J. Hydrog. Energy* **45** 23174–200

[23] Wietschel M *et al* 2021 *Metastudie Wasserstoff—Auswertung von Energiesystemstudien: Studien im Auftrag des Nationalen Wasserstoffrats* (Fraunhofer ISI, Fraunhofer ISE and Fraunhofer IE)

[24] Prinz R 2024 Forschungsprojekt SuperLink *110kV HTS-Kabel für die Energieversorgung von München (IX. ZIEHL-Vorträge)*

[25] Allais A *et al* 2024 SuperRail–world-first HTS cable to be installed on a railway network in France *IEEE Trans. Appl. Supercond.* **34** 1–7

[26] Airbus 2021 Cryogenics and superconductivity for aircraft, explained: ASCEND aims for a breakthrough in electric propulsion for aircraft (available at: www.airbus.com/en/newsroom/stories/2021-03-cryogenics-and-superconductivity-for-aircraft-explained) (Accessed 4 December 2025)

[27] Arndt T, Eisele M, Kläser M, Binder A, Köster R, Jöckel A, Zeichfüßl R and Krämer J 2026 Speedy_HTS—an HTS rotor for an uprated mid-speed wind power generator *IEEE Trans. Appl. Supercond.* **36** 1–4

[28] Mun H, Park S and Lee I 2023 Liquid hydrogen cold energy recovery to enhance sustainability: optimal design of dual-stage power generation cycles *Energy* **284** 129229

[29] Demaco Cryogenics 2023 The versatility of cryogenics: 11 cryogenic applications (Demaco Holland B.V)

(available at: https://demaco-cryogenics.com/blog/the-versatility-of-cryogenics-11-cryogenic-applications/) (Accessed 4 December 2025)
[30] Daimler Truck A G 2023 Daimler truck #HydrogenRecordRun: Mercedes-Benz GenH$_2$ truck cracks 1,000 kilometer mark with one fill of liquid hydrogen (available at: www.daimlertruck.com/en/newsroom/pressrelease/daimler-truck-hydrogenrecordrun-mercedes-benz-genh2-truck-cracks-1000-kilometer-mark-with-one-fill-of-liquid-hydrogen-52369346) (Accessed 4 December 2025)
[31] Hydrogen Energy Supply Chain 2022 About the project (available at: www.hydrogenenergysupplychain.com/about-hesc/) (Accessed 4 December 2025)
[32] Jordan T and Saw J L 2018 *Pre-normative REsearch for Safe use of Liquid Hydrogen (PRESHLY): White Paper* (Fuel Cells and Hydrogen Joint Undertaking)
[33] Alekseev A *et al* 2023 Hydrogen liquefaction, storage, transport and application of liquid hydrogen *Flagship Project TransHyDE* (https://doi.org/10.5445/IR/1000168281)
[34] Vysotsky V S, Nosov A A, Fetisov S S, Svalov G G, Kostyuk V V, Blagov E V, Antyukhov I V, Firsov V P, Katorgin B I and Rakhmanov A L 2013 Hybrid energy transfer line with liquid hydrogen and superconducting MgB_2 cable—first experimental proof of concept *IEEE Trans. Appl. Supercond.* **23** 5400906
[35] Vysotsky V S *et al* 2015 New 30-m flexible hybrid energy transfer line with liquid hydrogen and superconducting MgB_2 cable—development and test results *IEEE Trans. Appl. Supercond.* **25** 1–5
[36] Chen J, Zhang G, Qiu Q, Chen X, Teng Y, Jing L and Song N 2020 Simulation and experiment on superconducting DC energy pipeline cooled by LNG *Cryogenics* **112** 103128
[37] Xiao L 2023 *The Prospect of Carbon-Neutrality-Driven Energy & Power and the Possible Application of Superconductor* (Institute of Electrical Engineering Chinese Academy of Sciences)
[38] Fuhry F, Neumann H, Weiss K-P and Wolf M J 2025 Transport und Nutzung von flüssigem Wasserstoff: leitprojekt TransHyDE—Projekt AppLHy! *Chem. Ing. Tech.* **97** 145–55
[39] Peschka W 1992 *Liquid Hydrogen: Fuel of the Future* (Springer)
[40] Butting CryoTech GmbH 2020 Vacuum insulated piping (VIP): for common cryogenic media (available at: www.butting-cryotech.com/en/standard-transfer) (Accessed 4 December 2025)
[41] ITP Interpipe 2025 Cryogenic pipelines (available at: www.itp-interpipe.com/efficient-pipeline-solutions-for-extreme-temperature-fluids/cryogenic-pipelines/) (Accessed 4 December 2025)
[42] Markowz G, Dylla A and Elliger T 2010 icefuel®—an infrastructure system for cryogenic hydrogen storage, distribution and decentral use *Proc./18th World Hydrogen Energy Conf. 2010—WHEC 2010: Proc. (Schriften Des Forschungszentrums Jülich : Reihe Energie & Umwelt* vol 78) ed D Stolten (Forschungszentrum Jülich, Zentralbibliothek) pp 365–71
[43] Moore T 2002 SuperGrid concept sparks interest (available at: https://phe.rockefeller.edu/PDF_FILES/SuperGridSummary.pdf) (Accessed 4 December 2025)
[44] Grant P M 2004 The SuperCable: dual delivery of hydrogen and electric power *IEEE PES Power Systems Conf. and Exposition*
[45] Prats Campmany F 2021 Economical study of electric power transmission with superconducting lines for HVDC systems: memòria *Bachelor's Thesis* Escola Tècnica Superior d'Enginyeria Industrial de Barcelona
[46] Qin B, Wang H, Liao Y, Liu D, Wang Z and Li F 2024 Liquid hydrogen superconducting transmission based super energy pipeline for Pacific Rim in the context of global energy sustainable development *Int. J. Hydrog. Energy* **56** 1391–6
[47] Qin B, Wang H, Liao Y, Li H, Ding T, Wang Z, Li F and Liu D 2024 Challenges and opportunities for long-distance renewable energy transmission in China *Sustain. Energy Technol. Assess.* **69** 103925
[48] Wang L, Bai G, Zhang R and Liang J 2019 Concept design of 1 GW LH_2-LNG-superconducting energy pipeline *IEEE Trans. Appl. Supercond.* **29** 1–2
[49] Jin J, Wang L, Yang R, Zhang T, Mu S and Zhou Q 2022 A composite superconducting energy pipeline and its characteristics *Energy Rep.* **8** 2072–84
[50] Trevisani L 2006 Design and simulation of a large scale energy storage and power transmission system for remote renewable energy sources exploitation *Dissertation* Department of Electrical Engineering, University of Bologna (available at: http://die.ing.unibo.it/dottorato_it/Trevisani/Trevisani_PhD-thesis.pdf) (Accessed 4 December 2025)
[51] Yamada S, Hishinuma Y, Uede T, Schippl K and Motojima O 2008 Study on 1 GW class hybrid energy transfer line of hydrogen and electricity *J. Phys.: Conf. Ser.* **97** 12167
[52] Savoldi L, Balbo A, Bruzek C E, Grasso G, Patti M and Tropeano M 2024 Conceptual design of a SuperConducting energy pipeline for LH_2 and power transmission over long distances *IEEE Trans. Appl. Supercond.* **34** 1–5
[53] Bracco M *et al* 2025 Design of a submarine 30-km MgB_2 cable for the combined transfer of 0.3 GWe and LH_2 from offshore plants to the Ravenna port *IEEE Trans. Appl. Supercond.* **35** 1–6
[54] Bruzek C E *et al* 2024 MgB_2-based MVDC superconducting power cable in liquid hydrogen for hybrid energy distribution *IEEE Trans. Appl. Supercond.* **34** 1–5
[55] Mimmi F, Guerra E, Simonazzi M, Morandi A, Melaccio U and Bruzek C-E 2025 Comparative analysis of MgB_2 cable layouts for 1 GW superconducting transmission-insights from the SCARLET project *IEEE Trans. Appl. Supercond.* **35** 1–12
[56] Wimbush S and Strickland N 2019 Critical current characterisation of THEVA Pro-Line 2G HTS superconducting wire: figshare (Accessed 4 December 2025) (https://doi.org/10.6084/m9.figshare.3759327.v2)
[57] Braccini V, Nardelli D, Penco R and Grasso G 2007 Development of ex situ processed MgB_2 wires and their applications to magnets *Physica C* **456** 209–17
[58] Fu L, Chen X, Chen Y, Jiang S and Shen B 2024 Hydrogen-electricity hybrid energy pipelines for railway transportation: design and economic evaluation *Int. J. Hydrog. Energy* **61** 251–64
[59] Bundesnetzagentur 2025 Anbindungs-leitungen in der Nordsee (available at: https://www.netzausbau.de/Vorhaben/ansicht/de.html?nummer=1001&gruppe=offshore) (Accessed 4 December 2025)
[60] Bundesnetzagentur 2024 *Heide West—Polsum (Korridor B)* (available at: www.netzausbau.de/Vorhaben/ansicht/de.html?nummer=48&gruppe=bbplg) (Accessed 4 December 2025)
[61] TenneT TSO GmbH 2024 *Netzverstärkung NordElbe* (available at: www.tennet.eu/de/projekte/netzverstaerkung-nordelbe) (Accessed 4 December 2025)

[62] TenneT TSO GmbH 2023 *Die West-küstenleitung: das Projekt auf einen Blick* (available at: https://tennet-drupal.s3.eu-central-1.amazonaws.com/default/2023-11/Westk%C3%BCstenleitung%20Doppelparallelfalz.pdf) (Accessed 4 December 2025)

[63] Deutsche Energy Terminal GmbH 2024 Brunsbüttel (available at: https://energy-terminal.de/de/terminals/brunsbuettel) (Accessed 4 December 2025)

[64] Karres D 2025 Versorgung mit Flüssigerdgas LNG: Energiesicherheit (available at: https://www.kfw.de/stories/energiesicherheit_film.html) (Accessed 4 December 2025)

[65] Statistisches Bundesamt 2025 Größte Seehäfen in Deutschland in den Jahren von 2019 bis 2024 nach Güterversand: (in 1.000 Tonnen) (available at: https://de.statista.com/statistik/daten/studie/239219/umfrage/groesste-haefen-in-deutschland-nach-gueterversand/) (Accessed 4 December 2025)

[66] Flughafen Hamburg GmbH Corporate: all about Hamburg airport (available at: www.hamburg-airport.de/en/corporate) (Accessed 4 December 2025)

[67] Hamburger Hafen und Logistik Aktiengesellschaft The power of networks (available at: https://hhla.de/en/the-power-of-networks) (Accessed 4 December 2025)

[68] ArcelorMittal Germany Holding GmbH *Herzlich willkommen bei ArcelorMittal Hamburg* (available at: https://hamburg.arcelormittal.com/) (Accessed 4 December 2025)

[69] Färber A *Das Luftfahrtcluster der Metropolregion Hamburg* (available at: https://metropolregion.hamburg.de/wirtschaft-wissenschaft/branchen/luftfahrt-12722) (Accessed 4 December 2025)

[70] Airbus Airbus in Germany (available at: www.airbus.com/en/our-worldwide-presence/airbus-in-germany) (Accessed 4 December 2025)

[71] NXP Semiconductors NXP in Germany (available at: www.nxp.com/company/about-nxp/worldwide-locations/germany:GERMANY) (Accessed 4 December 2025)

[72] Färber A *Metropolregion Hamburg—Stark in der Chemieindustrie* (available at: https://metropolregion.hamburg.de/wirtschaft-wissenschaft/branchen/chemie-12708) (Accessed 4 December 2025)

[73] Statistisches Amt für Hamburg und Schleswig-Holstein 2025 *Metropolregion Hamburg* (available at: www.statistik-nord.de/zahlen-fakten/regionalstatistik-datenbanken-und-karten/metropolregion-hamburg) (Accessed 4 December 2025)

[74] Hamburg Behörde für Wirtschaft und Innovation 2022 *Green Hydrogen Hub Europe* (Hamburg als Drehkreuz für Wasserstoffimporte nach Deutschland und Europa)

[75] Institut der deutschen Wirtschaft Köln Consult GmbH 2022 *Potenziale der Wasserstoffwirtschaft in der Freien und Hansestadt Hamburg* (Studie für HIW Hamburg Invest Wirtschaftsförderungsgesellschaft mbH)

[76] Hamburger Senat 2024 *Fragenkatalog Wasserstoffstrategie für Industrie & Hafen: energiewendebeirat Hamburg* (available at: www.hamburg.de/resource/blob/963698/fd4e237f945e210c4bf1775bb56152d6/d-fragenkatalog-wasserstoffstrategie-ewb-data.pdf) (Accessed 4 December 2025)

[77] Hagart-Alexander C 2010 Temperature Measurement *Instrumentation Reference Book* 4th edn, ed W Boyes (Butterworth-Heinemann) ch 21, pp 269–326

[78] Geertsen C, Damour A, Grobbelaar W and Sainz Torrent A 2024 *Cryogenic Pipelines for Industrial Applications. Feedback from LNG Projects and Applications to Liquid Hydrogen* PTC 2024: ITP Interpipe

[79] Aldalur E, Suárez A and Veiga F 2022 Thermal expansion behaviour of Invar 36 alloy parts fabricated by wire-arc additive manufacturing *J. Mater. Res. Technol.* **19** 3634–45

[80] Michler T 2014 Influence of gaseous hydrogen on the tensile properties of Fe–36Ni INVAR alloy *Int. J. Hydrog. Energy* **39** 11807–9

[81] Mills R L and Edeskuty F J 1965 *Hydrogen embrittlement tests of cryogenic metals* (available at: www.osti.gov/servlets/purl/4583616) (Accessed 4 December 2025)

[82] TenneT *Technik: hier erhalten Sie einen Überblick über die eingesetzte Technik im Projekt SuedOstLink* (available at: www.tennet.eu/de/projekte/technik) (Accessed 4 December 2025)

[83] VDE Verband der Elektrotechnik Elektronik Informationstechnik e.V 2023 *Technische Anschlussregel Mittelspannung (VDE-AR-N 4110)* (available at: www.vde.com/de/fnn/themen/tar/tar-mittelspannung-vde-ar-n-4110) (Accessed 4 December 2025)

[84] Kuhn G 2020 *MVDC PLUS® Introduction: Siemens Energy Transmission Solutions (VDE Symp.)* (*Erfurt*)

[85] Morandi A 2015 HTS dc transmission and distribution: concepts, applications and benefits *Supercond. Sci. Technol.* **28** 123001

[86] Kalsi S S 2011 *Applications of High Temperature Superconductors to Electric Power Equipment* (IEEE Press)(https://doi.org/10.1002/9780470877890)

[87] Kottonau D *et al* 2020 *Evaluation of the Use of Superconducting 380 kV Cable* (KIT Scientific Publishing)(https://doi.org/10.5445/ksp/1000117918)

[88] Klöppel S, Marian A, Haberstroh C and Bruzek C-E 2021 Thermo-hydraulic and economic aspects of long-length high-power MgB_2 superconducting cables *Cryogenics* **113** 103211

[89] International Electrotechnical Commission 2017 *IEC 62895:2017. High Voltage Direct Current (HVDC) Power Transmission—cables with Extruded Insulation and Their Accessories for Rated Voltages up to 320 kV for Land Applications—test Methods and Requirements (Norme internationale/Commission Electronique Internationale, CEI)* vol 62895, 1st edn (International Electrotechnical Commission)

[90] Jefferies M J and Mathes K N 1970 Dielectric loss and voltage breakdown in liquid nitrogen and hydrogen *IEEE Trans. Electr. Insul.* **EI 5** 83–91

[91] Inoue N *et al* 2023 Test operation of 500 m /100 MW Ishikari high-temperature superconducting DC transmission line to demonstrate the required cost reduction and robustness *J. Phys.: Conf. Ser.* **2545** 12024

[92] Naumov A V *et al* 2014 Current leads and joints for HTS DC cable of 2.5 kA 20 kV *ADVANCES IN CRYOGENIC ENGINEERING: Trans. CRYOGENIC Engineering Conf.—CEC. AIP Conf. Proc.* (*Anchorage, Alaska, USA, 17–21 June 2013*) (AIP Publishing LLC) pp 1694–9

[93] Saugrain J-M 2017 Three years operation experience of the ampacity system installation in Essen, Germany

[94] Ross M 2023 Utility applications and experience with resilient electric grid systems utilizing high temperature superconductor wires in Chicago *Physica C* **614** 1354374

[95] Yang B, Kang J, Lee S, Choi C and Moon Y 2015 Qualification Test of a 80 kV 500 MW HTS DC cable for applying into real grid *IEEE Trans. Appl. Supercond.* **25** 1–5

[96] Wolf M, Wehr M, Palacios S and Arndt T 2024 Opportunities and challenges of using HTS REBCO in liquid hydrogen (LH_2) *4th Int. Workshop on Cooling Systems for High-temperature Superconductor Applications (IWC-HTS 2024)* (*Matsue, Japan*)

[97] Wolf M J *et al* 2022 200 kA DC busbar demonstrator DEMO 200—conceptual design of superconducting 20 kA busbar modules made of HTS CroCo strands *IEEE Trans. Appl. Supercond.* **32** 1–7

[98] Didier G, Bonnard C H, Lubin T and Lévêque J 2015 Comparison between inductive and resistive SFCL in terms of current limitation and power system transient stability *Electr. Power Syst. Res.* **125** 150–8
[99] Hust J G and Lankford A B 1984 *Thermal Conductivity of Aluminium, Copper, Iron, and Tungsten for Temperatures from 1 K to the Melting Point: NBSIR 84–3007* (National Bureau of Standards, U.S. Department of Commerce)
[100] Lee J A and Woods S 2016 *Hydrogen Embrittlement (JSC-CN-36009)*
[101] Rosskopf A and Brunner C 2022 Enhancing litz wire power loss calculations by combining a sparse strand element equivalent circuit method with a voronoi-based geometry model *IEEE Trans. Power Electron.* **37** 11450–6
[102] Sousa W T B D 2015 Transient simulations of superconducting fault current limiters *Tese (doutorado)* (COPPE, Universidade Federal do Rio de Janeiro)
[103] Butcher J C 2008 *Numerical Methods for Ordinary Differential Equations* (Wiley)
[104] Glisson T H 2011 Circuit elements, circuit diagrams, and Kirchhoff's Laws *Introduction to Circuit Analysis and Design* (Springer) pp 49–81
[105] Khonya A *System-Level Modeling of the Powertrain for an Electric Aircraft with Superconducting Components* (KIT Scientific Publishing) (https://doi.org/10.5445/KSP/1000181030)
[106] Trevisani L, Fabbri M and Negrini F 2007 Long distance renewable-energy-sources power transmission using hydrogen-cooled MgB_2 superconducting line *Cryogenics* **47** 113–20
[107] Ruck S 2025 *Thermofluiddynamik: Grundlagen, Theorie und Beispiele der konvektiven Wärmeübertragung bei laminaren und turbulenten Strömungen* (Springer) (https://doi.org/10.1007/978-3-658-48882-6)
[108] Flynn T M 2005 *Cryogenic Engineering* 2nd edn (Dekker)
[109] Herrmann P F, Cottevieille C, Duperray G, Leriche A, Verhaege T, Albrecht C and Bock J 1993 Cryogenic load calculation of high Tc current lead *Cryogenics* **33** 555–62
[110] Heller R, Fietz W H, Heiduk M, Hollik M, Kienzler A, Lange C, Lietzow R, Meyer I, Richter T and Vogel T 2018 Overview of JT-60SA HTS current lead manufacture and testing *IEEE Trans. Appl. Supercond.* **28** 1–5
[111] Belyadi H, Fathi E and Belyadi F 2017 Hydraulic fracturing chemical selection and design *Hydraulic Fracturing in Unconventional Reservoirs* ed H Belyadi (Gulf Professional Publishing) ch 8, pp 107–20
[112] Hussein A 2023 Flow assurance *Essentials of Flow Assurance Solids in Oil and Gas Operations* ed A Hussein (Gulf Professional Publishing) ch 2, pp 53–103
[113] Simpson D A 2017 Surface engineering concepts *Practical Onshore Gas Field Engineering* ed D A Simpson (Gulf Professional Publishing) ch 4 , pp 221–72
[114] Krempetz K, Grimson J and Kelly P 1986 *A Design Chart for Long Vacuum Pipes and Shells: TM-1378* (Fermi National Accelerator Laboratory)
[115] TenneT TSO GmbH and TransnetBW GmbH 2024 *SuedLink verstehen: Alles Wichtige zu Kabeln, Bauwerken und Genehmigungsverfahren*
[116] Wang A *et al* 2021 *Analysing Future Demand, Supply, and Transport of Hydrogen. European Hydrogen Backbone* (Guidehouse)
[117] Smith D R and Fickett F R 1995 Low-temperature properties of silver *J. Res. Nat. Inst. Stand. Technol.* **100** 119–71
[118] Lu J, Choi E S and Zhou H D 2008 Physical properties of hastelloy® C-276™ at cryogenic temperatures *J. Appl. Phys.* **103** 64908
[119] Mäder O 2012 *Simulationen und Experimente zum Stabilitätsverhalten von HTSL-Bandleitern* (KIT Scientific Publishing) (https://doi.org/10.5445/KSP/1000028713)
[120] Simon N J, Drexler E S and Reed R P 1992 Properties of copper and copper alloys at cryogenic temperatures *NIST Monograph* **177** 8–6
[121] Naito T, Fujishiro H, Yamamura Y, Saito K, Okamoto H, Hayashi H, Fujiwara N, Gosho Y and Shiohara Y 2011 Thermal conductivity of YBCO coated conductors reinforced by metal tape *IEEE Trans. Appl. Supercond.* **21** 3037–40
[122] Skonieczny M, Izdebska N, Królikowska M and Marczewski M 2024 Corrosion behaviour of aluminum and copper in dimethyl- and diethyl phosphate ionic liquids *Electrochim. Acta* **500** 144770
[123] Dirahoui W, Menana H, Hinaje M and Lévêque J 2022 Magnetothermal modeling of multilayer HTS tapes for quality control at room temperature *Physica C* **600** 1354101
[124] Lemmon E W, Bell I H, Huber M L and McLinden M O 2018 *REFPROP Documentation: Release 10.0* (National Institute of Standards and Technology)
[125] Haberstroh C 2024 Wasserstoff: ortho/Para-Umwandlung und Verflüssigung *Chem. Ing. Tech.* **96** 43–54